Aerodynamics and Impact Simulation of an Air-Dropped Ice Penetrator

by

Daniel Pekka Poe

B.S. Mechanical/Aerospace Engineering
Boston University, 2018

SUBMITTED TO THE DEPARTMENT OF AERONAUTICAL AND ASTRONAUTICAL ENGINEERING IN PARTIAL FULFILLMENT OF THE REQUIREMENTS FOR THE DEGREE OF

MASTERS OF SCIENCE IN AERONAUTICAL AND ASTRONAUTICAL AND ENGINEERING
at the
MASSACHUSETTS INSTITUTE OF TECHNOLOGY

JUNE 2021

© Massachusetts Institute of Technology 2021. All rights reserved.

Author.....
Department of Aeronautics and Astronautics
May 18, 2021

Certified by.....
Jeffrey Hoffman
Professor of Aeronautics and Astronautics
Thesis Supervisor

Accepted by.....
Zoltan Spakovszky
Professor of Aeronautics and Astronautics
Chair, Graduate Program Committee

Aerodynamics and Impact Simulation of an Air-Dropped Ice Penetrator

by

Daniel P. Poe

Submitted to the Department of Aeronautics and Astronautics
on May 18, 2021, in partial fulfillment of the
requirements for the degree of
Master of Science in Aeronautics and Astronautics

Abstract

In order to investigate movement of the Ross Ice Shelf in Antarctica, an air-dropped ice penetrator will be employed. Dropping a seismic probe from a helicopter offers several advantages over sending out a conventional crewed mission, such as reduced transit time and access to hard-to-reach locations. However, a new set of problems to be solved arises. The penetrator must fall fast enough to guarantee rigid coupling to the ice shelf, but slow enough to avoid damaging internal components. Aerodynamic analysis is used to select a penetrator geometry, and to suggest a drop altitude of at least 5000 ft (1524 m). Detailed simulations of the impact reveal shock loads up to 566 G from a drop velocity of 42.5 m/s. Finally, the effects of steady wind are analyzed, and point to a maximum recommended wind speed of 7.5 m/s for drop operations.

Thesis Supervisor: Jeffrey Hoffman
Title: Professor of Aeronautics and Astronautics

Acknowledgements

The author would like to acknowledge the National Science Foundation for funding this research. In particular, NSF Awards 1542950 "Development of an Air-droppable Goedetic-Seismic Ice Penetrator for Response Studies of Antarctic Ice Shelves and Icebergs to Ocean Forcings" and 1931131 "A New Instrument and Measurement Approach to Cryo-Seismogeodesy: Monitoring Antarctic Ice Shelf Stability Using Ice Penetrators" have made this work possible and are driving a new expedition to instrument the Antarctic cryosphere.

Professor Jeffrey Hoffman has shown unflinching patience when progress was slow, and steady encouragement when it sped up. He was always available to provide guidance when it was needed.

Dr. Pedro Elosegui also provided encouragement, was quick to reply to questions, and shared valuable resources over the course of this project.

Additional gratitude is due to Professor Katarina Miljkovic for providing her AUTODYN material model for water ice, to Professor Raul Radovitzky for his advice on the impact simulations, and to Professor Mark Drela for his input on the aerodynamic portion.

This research builds off of previous work done by Charlotte Lowey, Alice Cooper, and Madelyn Focaracci, all of whom built up a springboard that enormously accelerated the results attainable in these few years.

Finally, gratitude is due to Aily Walker for her support, proofreading sessions, and help deciphering a critical report written in Japanese.

Contents

1. Introduction 11
   1.1 Motivation 11
   1.2 Description of Penetrator 12
   1.3 Purpose of Aerodynamic Analysis 15
   1.4 Purpose of Impact Simulation 16
2. Background 17
   2.1 Military Penetrators 17
   2.2 Space-Based Penetrators 18
   2.3 Antarctic Penetrators 18
3. Aerodynamic Analysis 21
   3.1 Terminal Velocity 21
   3.2 Numerical Calculation 24
   3.3 Stability 26
   3.4 Assumptions 29
   3.5 Results 30
   3.6 Steady Wind Effects 35
4. Impact Simulation 39
   4.1 Problem Formulation in ANSYS 39
      4.1.1 Ice Model 39
      4.1.2 Snow Model 41
      4.1.3 Penetrator Material Models 46
   4.2 Speed Study 46
   4.3 Depth Study 54
   4.4 Wind-Induced Horizontal Velocity 62
      4.4.1 Helicopter Wind Speed Limitation 62
      4.4.2. Horizontal Velocity Impact Study 64
5. Matsushima Penetrator Comparison 75
6. Conclusion 81
   6.1 Summary 81
   6.2 Future Work 82

References 84

List of Figures

Figure 1-1. Crossing a crevasse near Prospect Point, Antarctica [2]. 11

Figure 1-2. Exploded view of single battery pack alongside stacked battery packs. 12

Figure 1-3. Seismometer housing in penetrator nosecone. 13

Figure 1-4. Schematic of penetrator at rest in snow pack. 14

Figure 1-5. Schematic of penetrator tipped into the wind at moment of impact. 15

Figure 2-1. Matsushima penetrator depth and AOA vs release height [14]. 19

Figure 2-2. Matsushima penetrator G load vs release height [14]. 19

Figure 2-3. ADIOS disk gap band parachute design [15]. 20

Figure 3-1. Calculating terminal velocity VT 22

Figure 3-2. Drag dynamics. 22

Figure 3-3. Adaptively refined mesh with 10^6 fluid cells. 24

Figure 3-4. Pressure contours with mesh and streamlines overlaid. 25

Figure 3-5. Velocity contours with mesh and streamlines overlaid. 25

Figure 3-6. Penetrator dimensions. 27

Figure 3-7. CP/CG locations for various flare geometries. Red box indicates geometry chosen for impact simulation. 31

Figure 3-8. Flare size required to set $\mathrm{VT} = 42.5\, m/s$ for various flare geometries. 32

Figure 3-9. AOA response for various flare geometries. 33

Figure 3-10. Schematic showing wind direction and lateral drag on penetrator. . 35

Figure 3-11. Vx/Vw vs altitude. 36

Figure 3-12. Penetrator trajectories w/nonzero drop velocity, zero wind. 37

Figure 3-13. Penetrator trajectories w/ helicopter flying into 7.5 m/s headwind. 38

Figure 4-1. Snow overburden pressure vs depth [20]. 41

Figure 4-2. Snow density vs depth [20]. 42

Figure 4-3. Snow elastic modulus vs density [21]. 43

Figure 4-4. Poisson's ratio of snow vs density [22]. 43

Figure 4-5. Log density vs log tensile strength of snow [23]. 44

Figure 4-6. Snow yield stress, pressure, shear modulus, and density. 44

Figure 4-7. Speed of sound through snow vs density [24]. 45

Figure 4-8. CAD model of impact assembly for speed study. 47

Figure 4-9. Density profile of snow in Marie Byrd Land [27]. 47

Figure 4-10. Vertical position, velocity, and G load for $V = 20m/s$, 10 cm ice layer. 48

Figure 4-11. Vertical position, velocity, and G load for $V = 30m/s$, 10 cm ice layer. 48

Figure 4-12. Vertical position, velocity, and G load for $V = 40m/s$, 10 cm ice layer. 49

Figure 4-13. Vertical position, velocity, and G load for $V = 50m/s$, 10 cm ice layer. 49

Figure 4-14. Vertical position, velocity, and G load for $V = 20m/s$, no ice. 49

Figure 4-15. Vertical position, velocity, and G load for $V = 30m/s$, no ice. 50

Figure 4-16. Vertical position, velocity, and G load for $V = 40m/s$, no ice. 50

Figure 4-17. Vertical position, velocity, and G load for $V = 50m/s$, no ice. 50

Figure 4-18. Final resting depth of penetrator as function of drop velocity. 52

Figure 4-19. Max G load on flare as function of drop velocity. 53

Figure 4-20. CAD model of impact assembly for depth study. 54

Figure 4-21. Vertical position, velocity, and G load for $d = 0.5\,m$, 10 cm ice layer. 55

Figure 4-22. Vertical position, velocity, and G load for $d = 1\,m$, 10 cm ice layer. 55

Figure 4-23. Vertical position, velocity, and G load for $d = 1.5\,m$, 10 cm ice layer. 55

Figure 4-24. Vertical position, velocity, and G load for $d = 2\,m$, 10 cm ice layer. 56

Figure 4-25. Vertical position, velocity, and G load for $d = 0.5\,m$, 20 cm ice layer. 56

Figure 4-26. Vertical position, velocity, and G load for $d = 1\,m$, 20 cm ice layer. 57

Figure 4-27. Vertical position, velocity, and G load for $d = 1.5\,m$, 20 cm ice layer. 57

Figure 4-28. Vertical position, velocity, and G load for $d = 2\,m$, 20 cm ice layer. 57

Figure 4-29. Max flare G load vs flare velocity at impact. 59

Figure 4-30. Final resting depth of penetrator as function of ice layer depth..... 60

Figure 4-31. Max G load on flare as function of ice layer depth. 61

Figure 4-32. Payload and range capabilities of AS350-B3e and Bell 412 [29]. 62

Figure 4-33. Wind rating of AS350-B3e in hover [30]..... 63

Figure 4-34. Wind rating of Bell 412 in hover [31]. 63

Figure 4-35. Schematic of range of velocities considered for tipping study..... 64

Figure 4-36. 3D and 2D geometries considered for tipping study. 65

Figure 4-37. 3D and 2D meshes in ANSYS. 67

Figure 4-38. 3D ANSYS result, $VY = -42.5 m/s, VX = 2.5 m/s$. 67

Figure 4-39. 2D ANSYS result, $VY = -42.5 m/s, VX = 2.5 m/s$. 68

Figure 4-40. Angle off vertical during tipping. 68

Figure 4-41. Penetrator angle for 3D and 2D cases, $VX = 2.5 m/s$. 69

Figure 4-42. Penetrator angle for 3D and 2D cases, $VX = 5 m/s$. 70

Figure 4-43. Penetrator angle for 3D and 2D cases, $VX = 7.5 m/s$. 70

Figure 4-44. Penetrator angle for 3D and 2D cases, $VX = 10 m/s$. 70

Figure 4-45. Penetrator angle for 3D and 2D cases, $VX = 15 m/s$. 71

Figure 4-46. Penetrator angle for 3D and 2D cases, $VX = 20 m/s$. 71

Figure 4-47. Penetrator angle for 3D and 2D cases, $VX = 30 m/s$. 71

Figure 4-48. Max difference between $\theta 3D$ and $\theta 2D$ occurring before $t = 0.06\, s$.. 72

Figure 4-49. Meteoblue wind model for McMurdo Station [33]. 73

Figure 5-1. Details of Matsushima penetrator geometry [14]..... 75

Figure 5-2. CAD recreation of Matsushima penetrator. 76

Figure 5-3. SolidWorks Flow Simulation mesh for Matsushima penetrator..... 77

Figure 5-4. Pressure contours for Matsushima penetrator at 60 m/s. 77

Figure 5-5. Drag vs velocity for Matsushima penetrator. 78

Figure 5-6. Matsushima impact geometry and axisymmetric mesh. 79

Figure 5-7. Position, velocity, and acceleration for 200 m drop altitude. 79

Figure 5-8. Position, velocity, and acceleration for 149 m drop altitude. 80

List of Tables

Table 3-1. Assumptions inherent in Barrowman's equations. 29

Table 3-2. 2% settling times (sec) for various flare geometries. 30

Table 3-3. Total penetrator mass (kg) for various flare geometries. 34

Table 4-1. Johnson-Cook strength model for ice [19]. 40

Table 4-2. Polynomial EOS for ice [19]. 40

Table 4-3. Failure model for ice [19]. 40

Table 4-4. Mass, volume, and density of penetrator ANSYS model 46

Table 4-5. Final depth, flare impact velocity, and max G load for 10 cm ice layer. 51

Table 4-6. Final depth, flare impact velocity, and max G load for no ice layer. . 51

Table 4-7. Final depth, flare impact velocity, and max G load for 10 cm ice layer. 58

Table 4-8. Final depth, flare impact velocity, and max G load for 20 cm ice layer. 58

Table 4-9. 2D mass and volume scaling for tipping study. 66

Table 5-1. Conditions of Matsushima penetrator drops [14]. 76

Table 5-2. Drop altitude and impact velocity of Matsushima penetrator. 78

Table 5-3. Matsushima impact [14] and ANSYS comparison. 80

1. Introduction

1.1 Motivation

Instrumenting the Ross Ice Shelf with seismometers and GPS trackers provides critical data on ice shelf dynamics. As ice flows from over land onto the shelf, it displaces seawater and contributes to the rise of ocean levels worldwide. In a perfect equilibrium, the ice flow is perfectly balanced by net evaporation from the ocean surface, but such a balance may no longer hold in an era of rapid climate change. GPS position and seismic data can paint a vivid picture of ice shelf behavior and changing trends in the Antarctic hydrosphere.

Given the scale of the Ross Ice Shelf, a crewed mission to install the sensors would involve traversing vast distances over terrain pockmarked with crevasses [1]. Air-dropping a penetrator with an integrated seismometer and GPS antenna avoids a costly and potentially dangerous crewed mission while dramatically increasing the range accessible for instrument placement.



Figure 1-1. Crossing a crevasse near Prospect Point, Antarctica [2].

1.2 Description of Penetrator

The mission of the penetrator is to record seismic activity and GPS location, and transmit both data sets continuously for one year via the Iridium satellite network. The penetrator will be air-dropped into the Ross Ice Shelf via helicopter, left in place for one year, and collected in order to abide by the Protocol on Environmental Protection to the Antarctic Treaty. Power for the telemetry antenna will be provided by internal primary batteries, which form the bulk of the penetrator body. The combined annual energy consumption of the telemetry antenna, GPS antenna, seismometer, and onboard electronics dictates the number of batteries required, and thus the overall size of the penetrator. The battery layout is shown below in Figure 1-2.

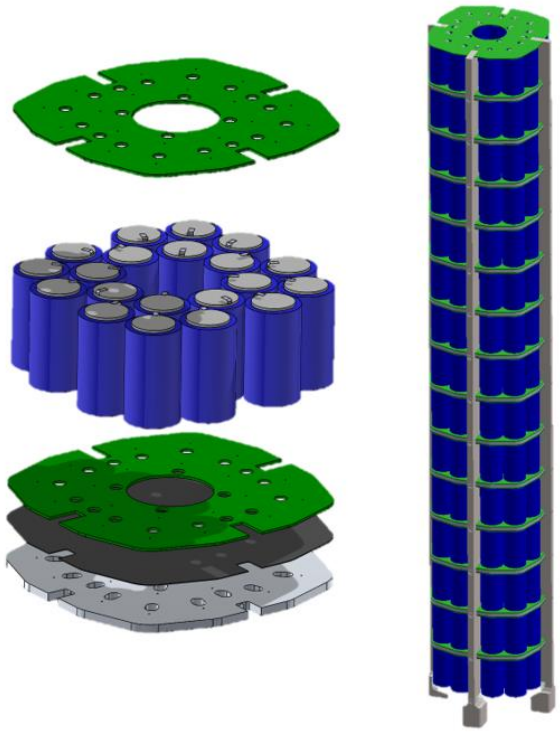


Figure 1-2. Exploded view of single battery pack alongside stacked battery packs.

Each battery pack houses 20 D-sized Lithium Thionyl Chloride (Li/SOCl2) primary batteries, chosen for their high energy density of 1112 Wh/kg and exceptional cold weather performance down to -60ºC [3]. The battery packs are 6.86 cm tall and 19.05 cm wide at the largest diameter. The packs can be stacked vertically into a 20 cm outer diameter cylinder which serves as the outer mold line of the penetrator body. Power draw testing conducted at Haystack Observatory

yielded an combined average draw of 2.435 W for all systems [4], translating to a requirement for the batteries to hold an initial 76.79 MJ of energy. At 68.4 Wh or 246,240 J per battery, a total of 312 batteries weighing 19 kg are needed to provide the energy. A margin of just over 20% brings the total number of batteries to 380, and the combined battery weight to 23.4 kg. A tightly packed stack of 380 batteries as shown in Figure 1-2 is 130 cm tall, but further aerodynamic and impact analysis will assume a 2-meter-long body section to allow for other structural elements and ample shock-absorbing material to be housed in the body section. The longer body section will also increase the aerodynamic stability of the penetrator in flight.

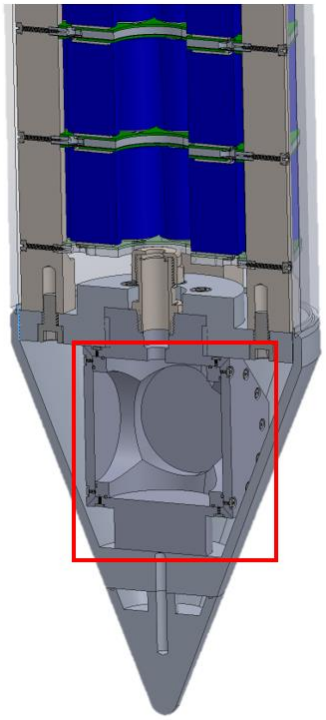


Figure 1-3. Seismometer housing in penetrator nosecone.

The nosecone of the body section houses the seismometer, and must embed itself firmly within the snow pack so that seismic waves are fully transferred to the instrument. The Trillium Compact 120s seismometer is chosen for its low power consumption of 180 mW, cold temperature operation down to -20ºC, small size of 1.2 kg, and relatively high shock tolerance of 100 G [5]. To reduce shock loading on the seismometer, the instrument could be mounted further up the body section with shock-absorbing material placed beneath.

The body section must penetrate 1 to 1.5 body lengths into the snow pack to ensure that the tail end does not protrude above the surface. If it does, winds could impart

movement to the seismometer, corrupting the sensitive seismic signal. However, the telemetry antenna must remain above the surface, in fact well above the surface given annual snowfall patterns on the Ross Ice Shelf. The antenna must be able to transmit freely for one year without interference from being buried underneath snow. The 1957-1958 Ross Ice Shelf traverse recorded a maximum annual snow accumulation rate of 64.5 cm/year [6], giving a lower bound for how high above the surface the antenna must stand after initial impact. In order to cover the possibility of significantly higher than expected snowfall, the antenna should stand about 1 to 1.5 meters above the surface. In order to meet the requirements for the antenna to stand above the surface and the penetrator body to emplace below the surface, a two-piece design consisting of a body section and an aft flare was adopted for the penetrator.

Upon impact, the aft flare will separate from the penetrator body. The body will penetrate into the snow pack, and the flare will come to rest on the surface. A schematic of the resting condition is shown below in Figure 1-4.

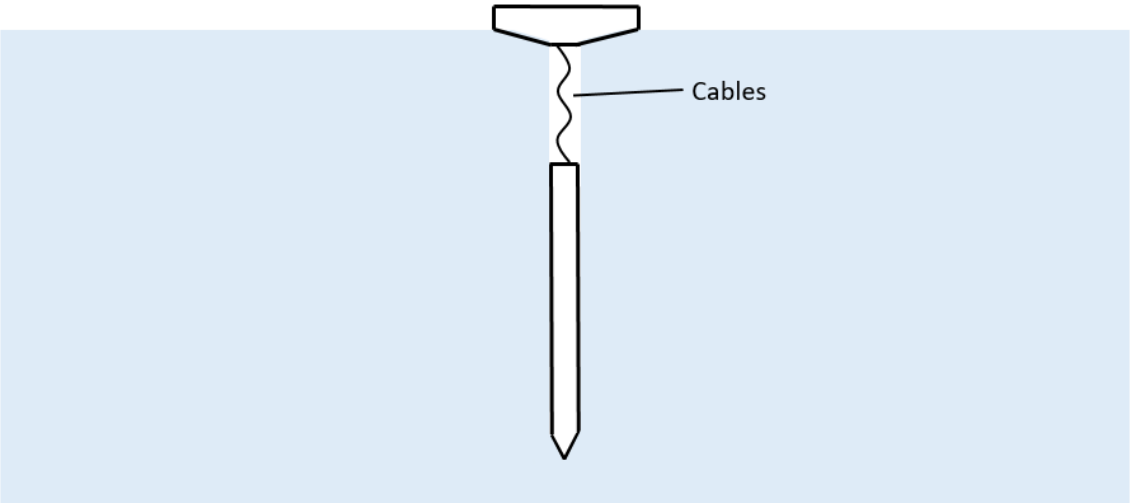


Figure 1-4. Schematic of penetrator at rest in snow pack.

Since the seismometer and batteries are housed in the body section and the GPS/telemetry antennae reside in the flare, cables for data and power must be routed from the body to the flare. The cables will be packed in a way to allow for tangle-free unraveling as the body and flare separate from each other. A structural cable may also be included as a safeguard against pulling the power and data cables taut.

1.3 Purpose of Aerodynamic Analysis

The purpose of the aerodynamic analysis is to hone in on certain flare geometries that result in a desired terminal velocity. Once a penetrator configuration is found to fall at the desired terminal velocity, its aerodynamic stability characteristics can be analyzed. Knowledge of the terminal velocity and aerodynamic stability informs the minimum drop altitude required for pitch oscillations to damp out, and maximizes the probability of the penetrator to impact the snow in a vertical orientation.

Wind effect are also considered, since wind may cause the penetrator to have a horizontal velocity component with an orientation other than vertical. In a worst-case scenario, the penetrator nose will be tipped into the wind, exacerbating the potential for the penetrator to tip over instead of burrow into the snow on impact.

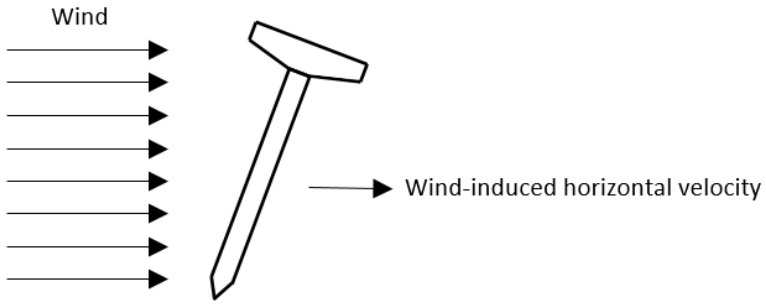


Figure 1-5. Schematic of penetrator tipped into the wind at moment of impact.

1.4 Purpose of Impact Simulation

The purpose of the impact simulations is to characterize the shock loads felt by the penetrator body and flare for various drop velocities. The flare is expected to experience higher G loading than the body since it comes to a rapid halt at the surface, but the body houses the sensitive seismometer only rated up to 100 G. If the body experiences G loads exceeding 100 G, the final penetrator design should incorporate shock-absorbing materials such as polyethylene cushions or aluminum crush core. Shock loading on the flare will be used to drive structural requirements for the GPS and telemetry antennae. From a shock loading standpoint, the drop velocity should be as low as possible. However, other factors prevent the drop velocity from becoming arbitrarily low.

The impact simulations also provide insight into the final resting depth of the body. The requirement of the body section to penetrate 1 to 1.5 body lengths into the snow pack is a main driver of the required drop velocity.

Finally, the effects of wind are considered once again. The aerodynamic wind results are used to define an initial condition for the impact event. Impact simulations involving wind-induced horizontal velocity enable a decision to be made on the maximum allowable wind speed for drop operations. The higher the drop velocity, the stronger the wind tolerated by the penetrator. Ultimately, the desired drop velocity is based off the shock loading felt by the body and flare, the required penetration depth, and the maximum wind speed that will not cause the penetrator to deviate excessively from a vertical orientation.

2. Background

Penetrators have been used for decades to deliver weapons and instruments to hard-to-reach locations. Lorenz covers a thorough history of penetrator applications ranging from military penetrators used in combat to scientific penetrators on deep space probes to an expedition to drop penetrators in Antarctica [7].

2.1 Military Penetrators

As with many technologies, penetrators enjoyed the defense industry's deep pockets for their early research and development, and later spread to civilian applications once they already had an established military presence. Lorenz credits Benjamin Robins as conducting one of the first rigorous studies of ground penetration dynamics for his studies on artillery projectiles. Robins' work in the mid-1700s concluded that penetration depth into a constant-strength target varies with the square of velocity due to kinetic energy dissipation during impact [7].

Jumping closer to the modern era, World War II saw significant development of penetrator-based munitions. Bombs began to be customized for the material of intended impact. Armor-penetrating weapons saw construction using hardened steels and thickened casings to smash through hard targets. Lorenz makes particular note of the British 5443 kg Tallboy and 10160 kg Grand Slam along with the American 19800 kg T-12 "earthquake bombs" designed to breach targets immune to smaller, conventional bombs. The earthquake bombs had greatly strengthened nose sections and were dropped from sufficient altitude to reach speeds close to Mach 1 [7]. Their kinetic energy alone would emplace them deep into a target, where detonation would occur seconds to minutes later. The explosion would blast open a temporary cavity, and the subsequent seismic shock and cavity collapse would be responsible for much of the overall damage caused [7,8].

Instrumented penetrators for surveillance gained traction in the decades following World War II, with the Igloo White project in Vietnam representing perhaps the most famous example [7,9,10]. The project saw tens of thousands of penetrators dropped around the Ho-Chi-Minh trail in order to detect Viet Cong activity. The most common penetrator used as part of Igloo White was the 1.3 m long Air-Delivered Seismic Intrusion Detector (ADSID) housing a seismic detector that

could pick up human footprints up to 30 m away [7]. The emergence of remote-sensing penetrators such as those developed during the Vietnam War laid the groundwork for scientific penetrators meant only to monitor physical phenomenon, not to destroy targets.

2.2 Space-Based Penetrators

Many projects to develop space-based penetrators have been undertaken, but so far, not a single one has achieved successful emplacement into a celestial body. Out of the dozens of proposed projects, most were cancelled before any resemblance of completion, and only two progressed all the way to the launch phase [4]. Both of these missions intended to send penetrator probes to Mars. The first, the Russian Mars 96 mission, suffered a launch failure over the Pacific Ocean and crashed somewhere near the west coast of South America [11]. The second mission, Deep Space 2, launched successfully in 1999, but contact was lost with the spacecraft right before entry into Mars' atmosphere [12]. If the two penetrator probes on board Deep Space 2 separated properly from the cruise stage, it is likely that they penetrated the Martian soil as intended, since they were designed to passively stabilize themselves in the atmosphere. Unfortunately, no data was received concerning the probes, so whether or not they deployed successfully is not known. Even if not successful, the two penetrators on Deep Space 2 are the only space-based penetrators to date to reach their destination. Space-based penetrators may yet have a bright future ahead, but so far, budget cuts along with the combined rigors of penetrator and spacecraft design have conspired to thwart even the best efforts. Nevertheless, icy moons such as Europa and Enceladus, comets, asteroids, and other solar system bodies remain enticing targets for possible future penetrator missions.

2.3 Antarctic Penetrators

A few expeditions have been made to emplace penetrators into the Antarctic cryosphere. In late 1990, a Japanese team dropped dummy penetrators from a height of 600 m at Asuka Station in order to measure the hardness parameter of the surface layer of snow resting on top of the Antarctic ice sheet [13].

Another Japanese expedition dropped around a dozen penetrators into the Mizuho Plateau in winter (Antarctic summer) 2001-2002, but could not record any seismic activity due to electrical issues [14]. However, they produced a plethora of useful

test data on the penetrator drops. A 14.5 kg penetrator dropped from altitudes between 74 and 565 m reached penetration depths from 75 to 180 cm into the snow. Altitudes below 400 m were found insufficient to damp out pitch oscillations, and the angle of attack at impact ranged from zero to 45 degrees. Figure 2-1 and Figure 2-2 below show the penetration depth, angle of attack at impact, and G loading on the penetrator for various drop altitudes.

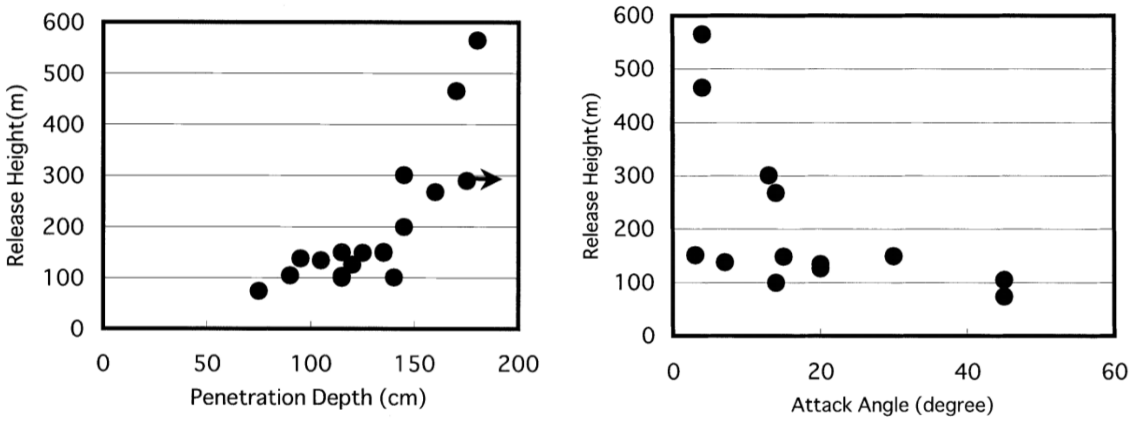


Figure 2-1. Matsushima penetrator depth and AOA vs release height [14].

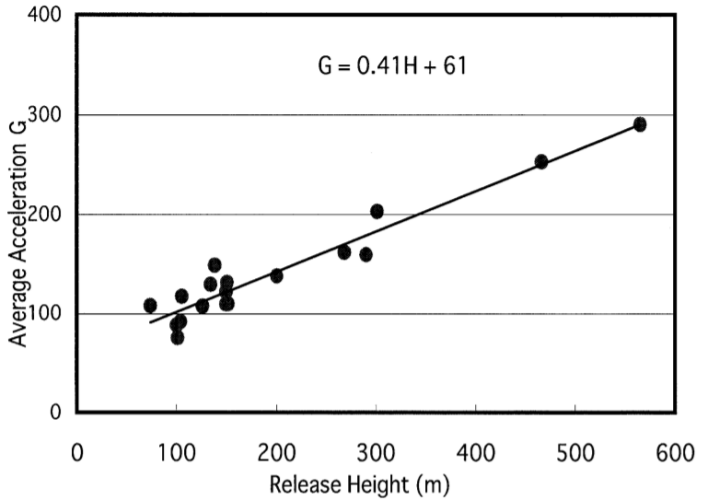


Figure 2-2. Matsushima penetrator G load vs. release height [14].

More recently, a British team deployed 37 penetrators to the Pine Island Glacier in Antarctica, of which 26 survived the drop [15]. The team attributes the high failure rate to the large number of crevasses in the target area. Their penetrator design, dubbed the Aircraft-Deployable Ice Observation System (ADIOS), incorporated a disk gap band parachute instead of a rigid airbrake like other penetrators.

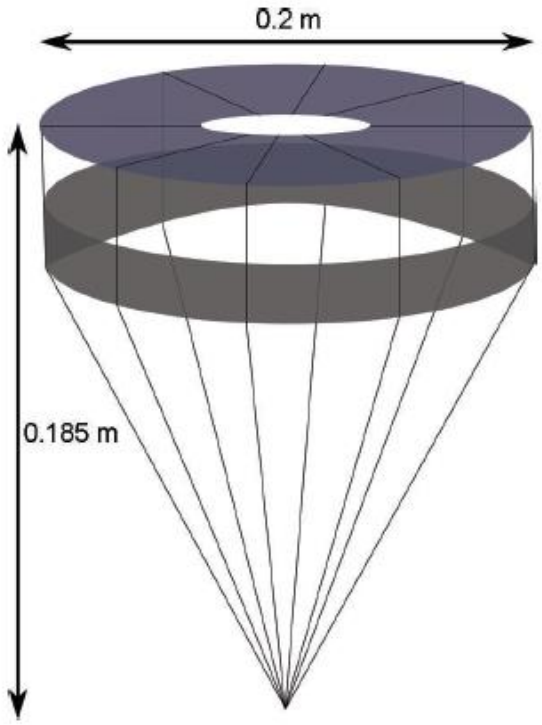


Figure 2-3. ADIOS disk gap band parachute design [15].

ADIOS was launched out of a sonobuoy tube mounted on a Twin Otter aircraft. After parachute deployment, ADIOS reached a terminal velocity of 42 m/s – almost identical to the terminal velocity considered in this study. The team expected to see impact shock loads up to 900 G, so their penetrator design incorporates a polyethylene cushion and a spring to insulate internal components from the harsh deceleration. Such shock absorbing materials may also prove necessary for the current penetrator design in consideration.

3. Aerodynamic Analysis

An air-dropped penetrator presents a unique aerodynamic problem – it must fall at a specific velocity, and it must be stable enough to guarantee a vertical orientation within set bounds on impact. The simplest way to guarantee a desired impact velocity is to select a geometry with terminal velocity equal to said impact velocity, and to drop the penetrator from a height sufficient to reach terminal velocity. There is no single solution to what geometry will cause a particular terminal velocity. Instead, a wide range of shapes may cause the same drag at particular speeds. Various penetrator geometries satisfying the V_T requirement may be studied in order to investigate the stability of each. In this analysis, the flare geometry is a truncated cone with an affixed aft cylinder, and the geometric parameters to be varied are the cone angle and cylinder depth.

3.1 Terminal Velocity

The main purpose of the aerodynamic analysis is twofold: to guarantee a desired terminal velocity, and to prove adequate aerodynamic stability during the drop. The desired terminal velocity must strike a balance between providing sufficient kinetic energy to securely embed the penetrator in the ice sheet while not providing enough to damage the electronics on impact. The maximum allowable deceleration of the seismometer places a limitation on excess drop velocity, and together with the requirement of the body tube to penetrate 1 to 1.5 body lengths into the ice, dictates a desired terminal velocity of 42.5 meters per second. Further rationale for selecting this velocity is given in Chapter 4. It should be noted that 42.5 m/s is not a value set in stone – it is merely one possible velocity that seems to satisfy the drop requirements. In order to achieve this relatively slow speed, a large conical flare serving as a drag-inducing air brake is affixed to the aft end of the penetrator. The process for honing in on the correct flare size is described below.

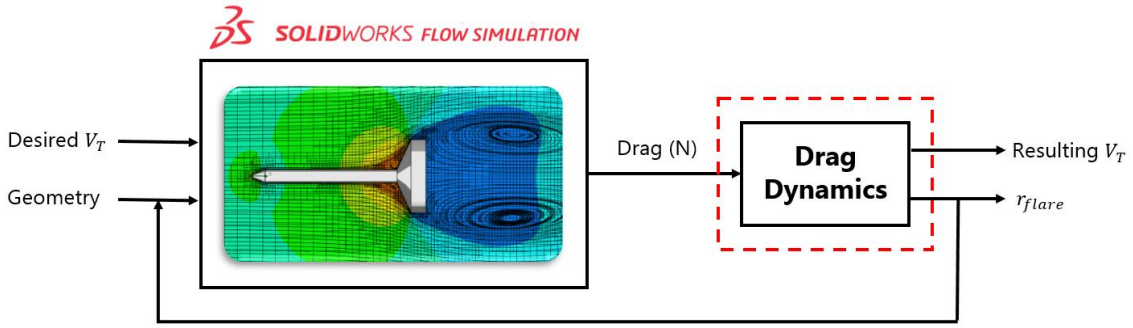


Figure 3-1. Calculating terminal velocity V_T.

An arbitrary flare radius is chosen, and the resulting drag is solved for computationally in SolidWorks Flow Simulation by simulating zero angle-of-attack airflow over the penetrator at 42.5 m/s. The drag and corresponding drag coefficient are used to calculate a new flare radius, which produces a new drag output from the solver. The process is repeated until the required drag at terminal velocity, equal to the total penetrator weight, differs from the numerically calculated drag by less than a preset tolerance, chosen to be 5 N due to limitations in the resolution of the CFD model. A 5 N discrepancy results in a maximum deviation in terminal velocity of less than 1 m/s.

The Drag Dynamics block in Figure 3-1 incorporates the drag equation in various forms, and is shown in more detail in Figure 3-2.

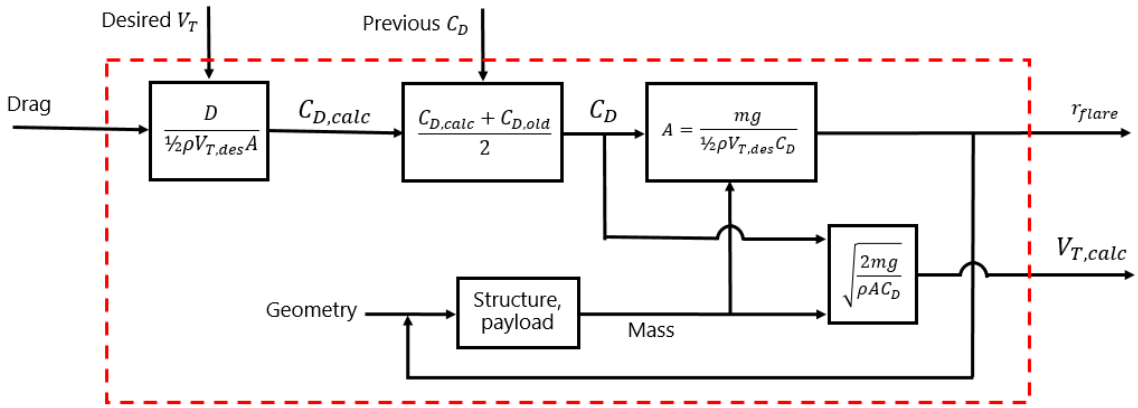


Figure 3-2. Drag dynamics.

The output of the SolidWorks CFD solver is a drag value given in Newtons. The desired terminal velocity is known, so once an initial estimate is provided for the flare radius, the drag D can be used to calculate a drag coefficient $C_{D,calc}$.

$$C_{D,calc} = \frac{D}{½\rho V_{T,des} A} \tag{3-1}$$

Here, ρ is the air density and $A = \pi r_{flare}^2$ is the cross-sectional area of the penetrator and flare seen by the airflow. In order to improve convergence stability, the calculated drag coefficient is averaged out with the drag coefficient of the previous run. The resulting average C_D is used to calculate a new flare radius r_{flare} via

$$A = \frac{mg}{½\rho V_{T,des} C_D} \tag{3-2}$$

where mg is the total penetrator weight. The new flare radius feeds back into the penetrator geometry, changing the flare mass and thus changing the required drag mg in equation 3-2. The updated drag produces a new flare radius, changing the mass yet again and forming an inner feedback loop that must converge before rerunning the CFD solver with the newly sized flare. Once C_D and r_{flare} are known, the resulting terminal velocity may be calculated by

$$V_{T,calc} = \sqrt{\frac{2mg}{\rho A C_D}} \tag{3-3}$$

3.2 Numerical Calculation

The mesh is adaptively refined in order to increase the fluid cell density only where it is most needed, striking a healthy compromise between solution accuracy and computational time required to solve. Starting out with a coarse, uniform mesh, SolidWorks Flow Simulation refines cells in areas of high pressure or velocity gradients as it works towards convergence. The maximum number of fluid cells is limited to 10^6 elements since further increases in cell count yield only marginal changes in calculated drag. At 10^6 elements, a 50% increase in maximum cell count changes drag by 5 N, or about 0.57%.

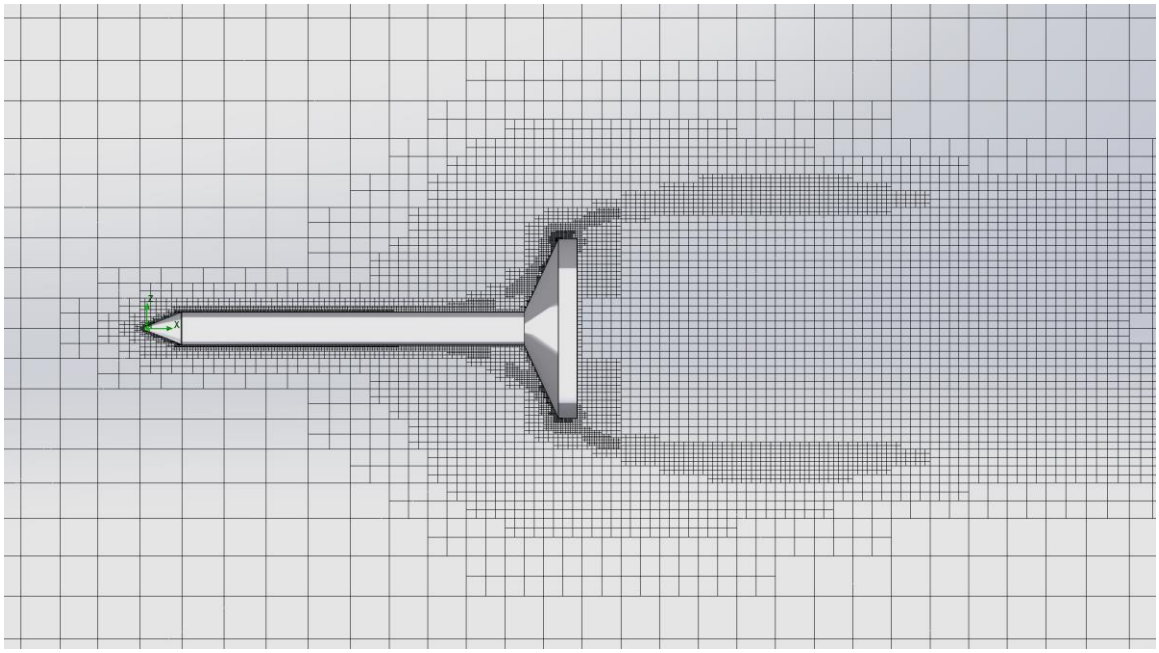


Figure 3-3. Adaptively refined mesh with 10^6 fluid cells.

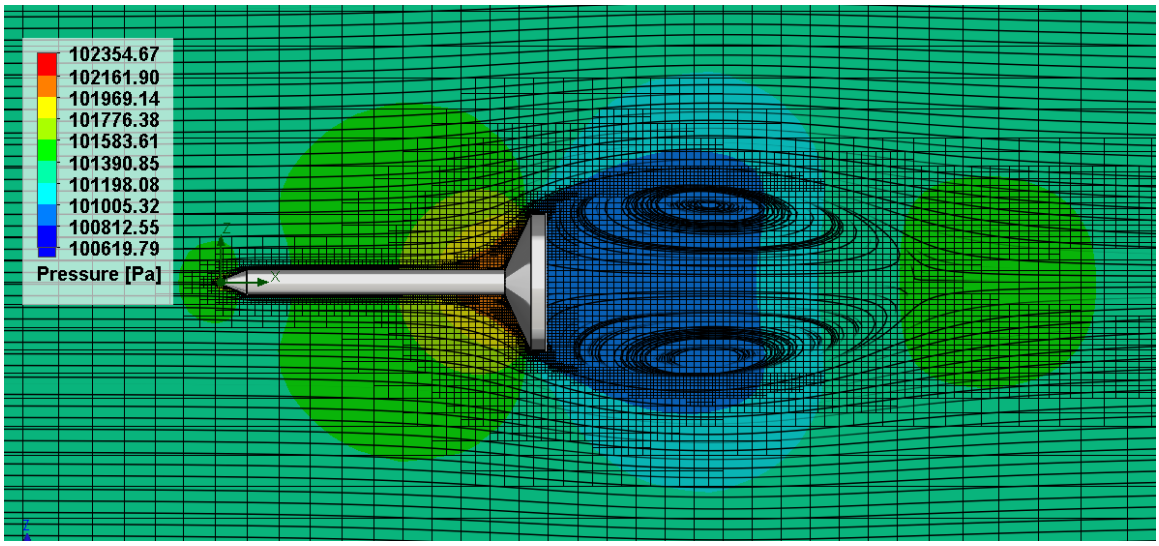


Figure 3-4. Pressure contours with mesh and streamlines overlaid.

As expected, the flare has a retarding and stabilizing effect on the penetrator. A large region of recirculation forms in the low-pressure zone trailing the flare, providing drag equal to the weight of the penetrator and pulling the center of pressure far aft of the center of mass. The mesh must be fine enough to capture complex flow interactions especially in the transition from the high pressure zone in front of the flare to the aft low pressure zone, but further away from the penetrator where the freestream flow is relatively undisturbed, a much coarser mesh is sufficient. For reference, the freestream flow velocity is 42.5 m/s.

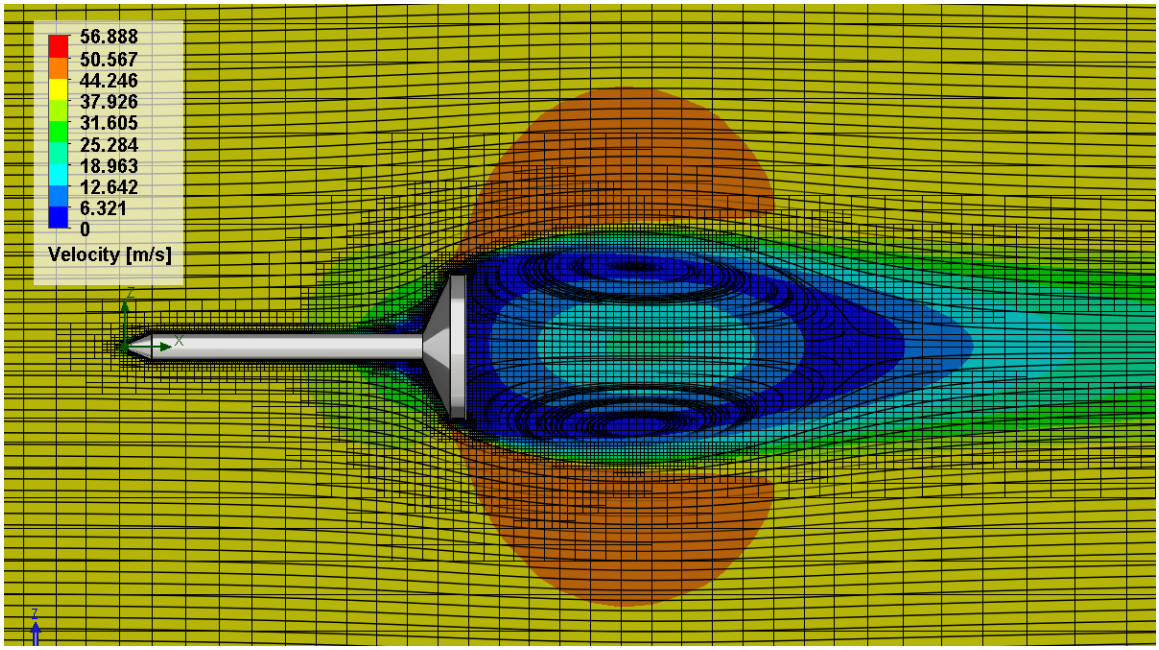


Figure 3-5. Velocity contours with mesh and streamlines overlaid.

3.3 Stability

Aerodynamic stability is analyzed using methods originally designed to describe the flight of model rockets. The two main differences between the penetrator and a rocket are the direction of flight with respect to the gravity vector, and the lack of propulsion as a non-aerodynamic influence on stability in the case of the penetrator. The methods for determining stability as outlined below only apply when deviations in angle of attack are small, with approximate error magnitudes growing from 1% for a 10 degree angle to 4% for a 20 degree angle. The analysis also makes several additional assumptions which are covered in detail in section 3.4. All equations and analysis in this section are based off of the Barrowman method as outlined by Mandell, Caporaso, and Bengen [16].

Barrowman describes the normal force coefficient C_{N_α} of a streamlined body as independent of cylindrical sections [16]; for the penetrator, only the nose cone and aft flare contribute since only they present a sizable cross-section to the airflow for small angles of attack.

$$C_{N_\alpha} = C_{N_\alpha,nose} + C_{N_\alpha,flare} \tag{3-4}$$

The nose contribution $C_{N_\alpha,nose}$ is equal to 2 regardless of shape [16], and the flare contribution $C_{N_\alpha,flare}$ is given by

$$C_{N_\alpha,flare} = 2\left(\frac{r_{flare}}{r_b} - 1\right)^2 \tag{3-5}$$

where r_{flare} and r_b are the widest and narrowest radii, respectively, of the flare. For reference, relevant penetrator dimensions are labeled in Figure 3-6 below.

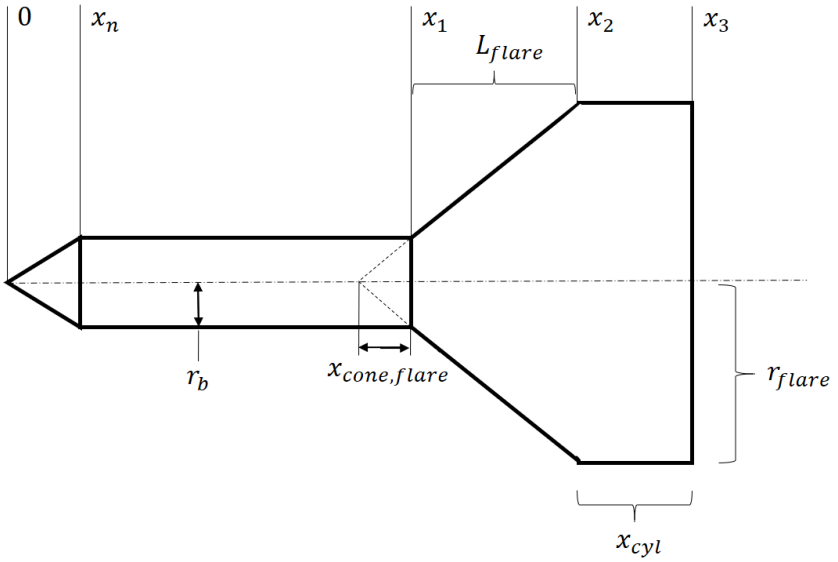


Figure 3-6. Penetrator dimensions.

The center of pressure of the conical nose is located on the centerline at a distance

$$\bar{x}_{nose} = \frac{2}{3}x_n \tag{3-6}$$

from the datum plane tangent to the nose cone tip. Conversely, the flare center of pressure can be found at the longitudinal coordinate

$$\bar{x}_{flare} = x_1 + L_{flare}\left(\frac{2}{3} - \frac{1}{3}\frac{r_b}{r_{flare}}\left(\frac{r_b}{r_{flare}} + 1\right)\right) \tag{3-7}$$

Using these quantities, the overall penetrator center of pressure is calculated by

$$\bar{x} = \frac{\left(C_{N_\alpha}\right)_{nose}\bar{x}_{nose} + \left(C_{N_\alpha}\right)_{flare}\bar{x}_{flare}}{C_{N_\alpha}} \tag{3-8}$$

Following the Barrowman method, Mandell, Caporaso, and Bengen define a corrective moment coefficient c_1 and a damping moment coefficient c_2 as

$$c_1 = \tfrac{1}{2}\rho V_T^2 A_r C_{N_\alpha}(\bar{x} - x_{CG}) \tag{3-9}$$

$$c_2 = \tfrac{1}{2}\rho V_T A_r\left[\left(C_{N_\alpha}\right)_{nose}(\bar{x}_{nose} - x_{CG})^2 + \left(C_{N_\alpha}\right)_{flare}\left(\bar{x}_{flare} - x_{CG}\right)^2\right] \tag{3-10}$$

and here it is important to note that the reference area A_r is the cross-sectional area of the body tube. c_1 and c_2 can be used to calculate the damping coefficient

D_c, natural frequency ω_n, damping ratio ζ, and damped natural frequency ω_d associated with the penetrator falling at terminal velocity. The parameters are given by

$$D_c = \frac{c_2}{2I_L} \tag{3-11}$$

$$\omega_n = \sqrt{\frac{c_1}{I_L}} \tag{3-12}$$

$$\zeta = \frac{D_c}{\omega_n} = \frac{c_2}{2\sqrt{c_1 I_L}} \tag{3-13}$$

$$\omega_d = \omega_n\sqrt{1-\zeta^2} = \sqrt{\frac{c_1}{I_L} - \frac{c_2^2}{4I_L^2}} \tag{3-14}$$

where I_L is the longitudinal moment of inertia of the penetrator. The damped natural frequency ω_d and the damping ratio ζ are of particular physical significance, since ω_d is the frequency at which the angle of attack of the penetrator will oscillate in flight, and ζ determines how many oscillations the penetrator will undergo before settling out.

3.4 Assumptions

Barrowman's equations make several assumptions as listed in Table 3-1. With the exception of one, all assumptions are met.

Table 3-1. Assumptions inherent in Barrowman's equations.

Assumption	Met	Rationale
The penetrator is a rigid body.	Y	To first order, the penetrator acts like a rigid body. The airframe is constructed of solid pieces of metal.
The penetrator is axially symmetric.	Y	While true CG location may shift slightly off of centerline due to internal components, the airframe is axially symmetric and the mass distribution will be as close to axially symmetric as possible.
The angle of attack is small.	Y	Variations in angle of attack will be caused by wind, which is much slower than the penetrator's vertical velocity.
Airflow over the penetrator is at steady state.	Y	Once the penetrator reaches terminal velocity, airflow will be at steady state.
Airflow over the penetrator is incompressible.	Y	The penetrator will fall at a terminal velocity of 42.5 m/s, corresponding to a Mach number of around 0.125.
Airflow over the penetrator is potential, i.e. inviscid and irrotational.	N	–

The final assumption is not met since the flare induces a significant amount of vorticity. However, it is worth noting that this assumption is almost never met in any application of Barrowman's equations. Model rockets also induce vorticity in their surrounding airflow, not to mention friction drag caused by viscous effects. Nevertheless, the equations serve as valid approximations, and the user should remain aware that the results will not represent the true aerodynamic response with exact accuracy.

3.5 Results

The outlined processes for calculating terminal velocity and stability associated were used to study a range of penetrator flare geometries. For ease of manufacturing, the flare design consists of a cylindrical section stacked on top of a conical section. Thus, the flare angle and cylinder depth are the only parameters with which to affect the flare geometry, and the effects of both parameters on the aerodynamic response of the penetrator were studied. The cylinder depth x_{cyl} ran from a range of 10% to 50% of the flare radius r_{flare}, and the flare angle θ ran from a range of 85 to 65 degrees as measured from the center axis.

The center of pressure C_P is an imaginary point through which the sum of all aerodynamic forces act, and it is a critical concept for stability analysis. In fact, the distance between the center of pressure and center of gravity is called the stability margin, a parameter that will guarantee stability if positive (C_P aft of C_G), and instability if negative (C_P forward of C_G). However, it is not purely a binary quantity; the higher a positive stability margin, the " more stable" the aerodynamic body, meaning that perturbations in angle of attack will damp out more quickly. Figure 3-7 shows the grid of all penetrator geometries studied along with a visual representation of the stability margin for each, and the red dashed box indicates the geometry chosen for subsequent impact simulation. Figure 3-8 shows the flare size for each penetrator geometry required to produce the required terminal velocity, while Figure 3-9 shows the stability characteristics in the form of the angle of attack response to an initial perturbation along with the damped natural frequency and damping ratio. Settling times for the response to decay to within 2% of the final value are catalogued in Table 3-2, which makes clear that the settling times depend more strongly on cylinder depth than they do on flare angle.

Table 3-2. 2% settling times (sec) for various flare geometries.

		Flare angle θ (deg)				
		85	**80**	**75**	**70**	**65**
x_{cyl} (m)	$\mathbf{0.1}r_{flare}$	16.14	15.64	15.59	15.57	15.25
	$\mathbf{0.2}r_{flare}$	17.45	17.13	17.15	17.10	17.14
	$\mathbf{0.3}r_{flare}$	19.24	19.17	18.90	19.14	19.34
	$\mathbf{0.4}r_{flare}$	21.44	21.33	21.46	21.75	22.26
	$\mathbf{0.5}r_{flare}$	24.19	24.23	24.45	24.96	26.03

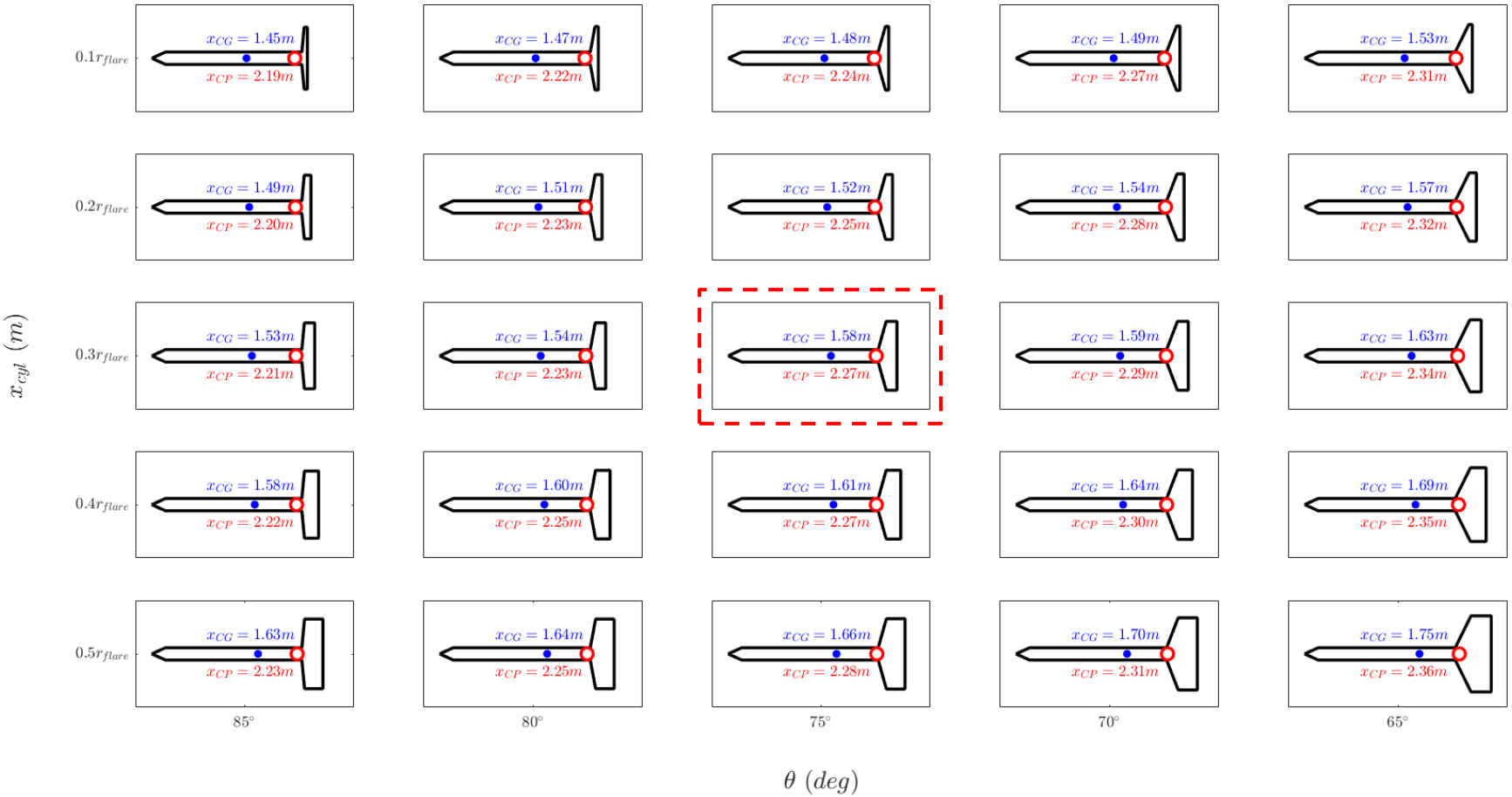


Figure 3-7. C_P/C_G locations for various flare geometries. Red box indicates geometry chosen for impact simulation.

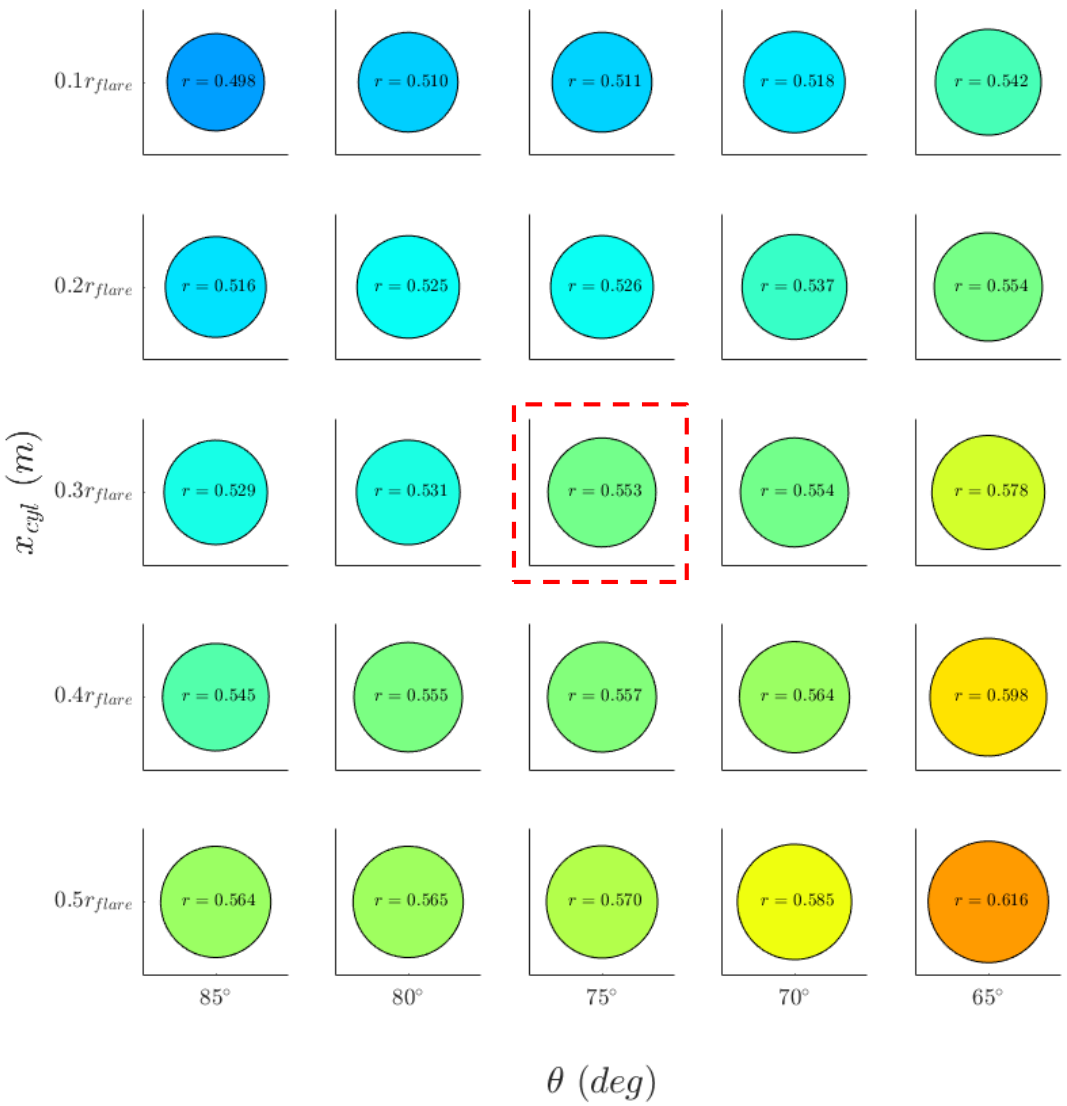


Figure 3-8. Flare size required to set $V_T = 42.5\, m/s$ for various flare geometries.

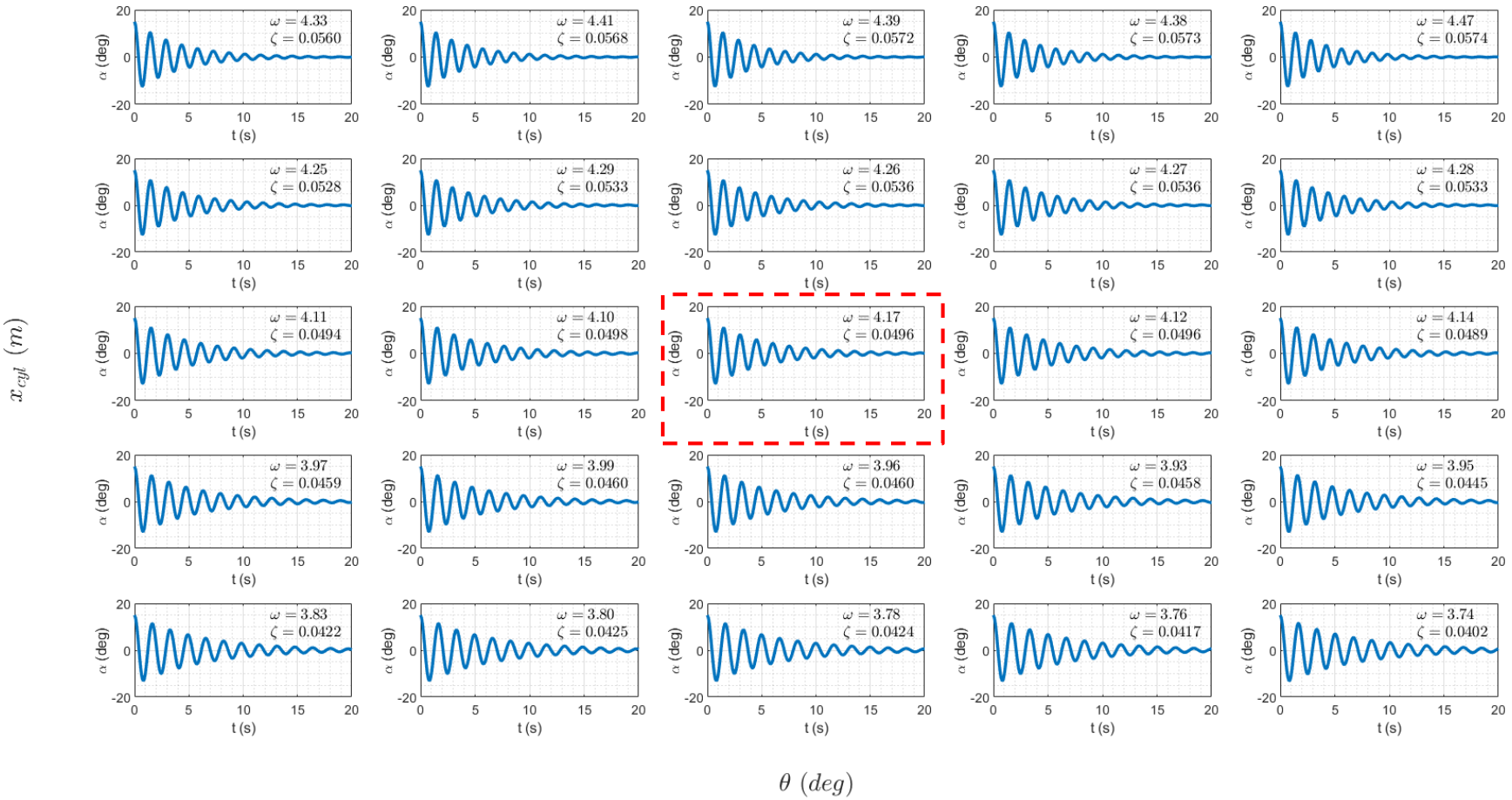


Figure 3-9. AOA response for various flare geometries.

Since the penetrator flight path is near vertical, pitch changes do not lead to the persistent, oscillating trade-off of potential and kinetic energy characteristic of a flight path with a horizontal component, and thus the aerodynamic response has only one mode. In aviation language, no Phugoid mode is present. Instead, the penetrator only shows the short period response, physically corresponding to "weathervaning" into the wind. Figure 3-7 and Figure 3-9 reveal that although a larger flare will pull the C_P aft, the additional mass will shift the C_G aft by a greater degree and thus reduce the stability margin. From a pure aerodynamic standpoint, a smaller flare size seems ideal, but this must be balanced with the physical size limitations of the equipment stored in the flare.

Each penetrator geometry has a slightly different mass, with the larger flares corresponding to higher masses. All penetrator mass values are tabulated below.

Table 3-3. Total penetrator mass (kg) for various flare geometries.

		Flare angle θ (deg)				
		85	**80**	**75**	**70**	**65**
$x_{cyl}\ (m)$	$\mathbf{0.1}r_{flare}$	81.92	82.87	83.08	84.06	86.22
	$\mathbf{0.2}r_{flare}$	85.70	86.41	86.96	88.23	90.24
	$\mathbf{0.3}r_{flare}$	89.44	89.95	92.22	92.44	95.57
	$\mathbf{0.4}r_{flare}$	93.81	94.97	95.66	96.84	100.95
	$\mathbf{0.5}r_{flare}$	99.11	99.29	100.33	102.42	106.96

The penetrator mass distribution assumes that internal penetrator components have a combined mass of 45 kg. Of the 45 kg total, 23.4 kg are allocated for batteries, 1.2 kg for the seismometer, and 20.4 kg for avionics, antennae, the seismometer gimbal, and other internal structure. The rest of the mass is taken up by the external penetrator skin, assumed to be 2 mm thick stainless steel.

3.6 Steady Wind Effects

For the steady wind analysis, the penetrator is considered to pitch into any relative wind instantaneously. Under this assumption, the longitudinal axis of the penetrator is always pointed directly into the relative wind, such that the penetrator's angle of attack is always zero even if the pitch angle is nonzero. For any nonzero pitch angle, a lateral drag is generated that strives to match the penetrator's horizontal velocity to that of the wind. Assuming that the wind velocity is low compared to the penetrator's vertical velocity, the lateral drag on the penetrator can be calculated by

$$D_x = \frac{mg(V_w - V_x)}{V_T} \tag{3-15}$$

where V_w is the absolute wind velocity, V_x is the penetrator's horizontal velocity, and V_T is the penetrator's terminal velocity. Once the penetrator's horizontal velocity equalizes with the wind velocity, $V_w - V_x$ and hence D_x drops to zero, and the penetrator's orientation becomes vertical.

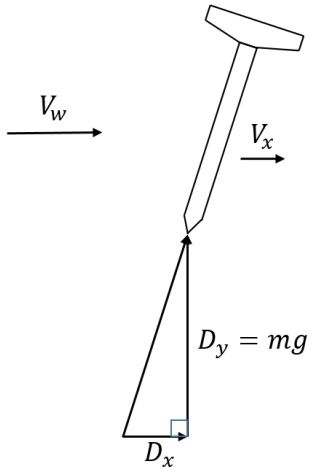


Figure 3-10. Schematic showing wind direction and lateral drag on penetrator.

D_x can be used to numerically integrate the horizontal velocity as a function of time. The horizontal velocity as a fraction of wind velocity is plotted against penetrator altitude in Figure 3-11.

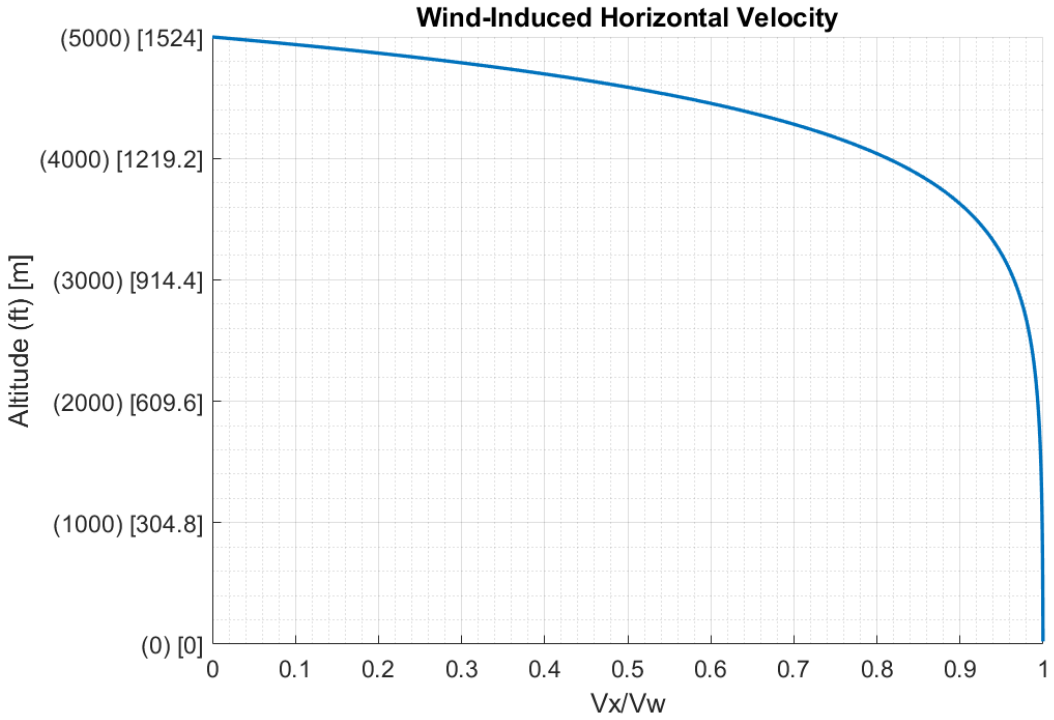


Figure 3-11. V_x/V_w vs. altitude.

After falling the first 1000 feet, the penetrator picks up just over 80% of the wind velocity. After the next 1000 feet, the penetrator's horizontal velocity reaches over 96% of the wind velocity, and after a total fall of 3000 ft, the horizontal velocity exceeds 99% of the wind velocity – equal for all practical purposes.

In case the helicopter elects to drop the penetrator from a cruise condition instead of from hover, an initial horizontal velocity is also considered. Dropping from hover in the presence of wind may seem computationally identical to dropping with an initial horizontal velocity in a zero-wind condition, but a different approach must be taken since the horizontal velocities involved are no longer small compared to the penetrator's terminal velocity. Again assuming that the longitudinal axis of the penetrator points directly into the relative wind, the horizontal and vertical forces are given by

$$F_x = \tfrac{1}{2}\rho V^2 \pi r_{flare}^2 C_D \frac{|V_x|}{V} \qquad 3\text{-}16$$

$$F_y = -mg + \tfrac{1}{2}\rho V^2 \pi r_{flare}^2 C_D \frac{|V_y|}{V} \qquad 3\text{-}17$$

where the total airspeed V is equal to $\sqrt{V_x^2 + V_y^2}$. V_x and V_y are the respective horizontal and vertical airspeed components. The drag coefficient C_D is assigned a constant value of 0.851, equal to that found for the penetrator with a 75° flare cone angle and a cylinder depth of $0.3r_{flare}$ (marked with the red box in Figure 3-7). A resulting set of trajectories is shown below in Figure 3-12. Here, V_d represents the horizontal velocity of the helicopter at the moment of drop.

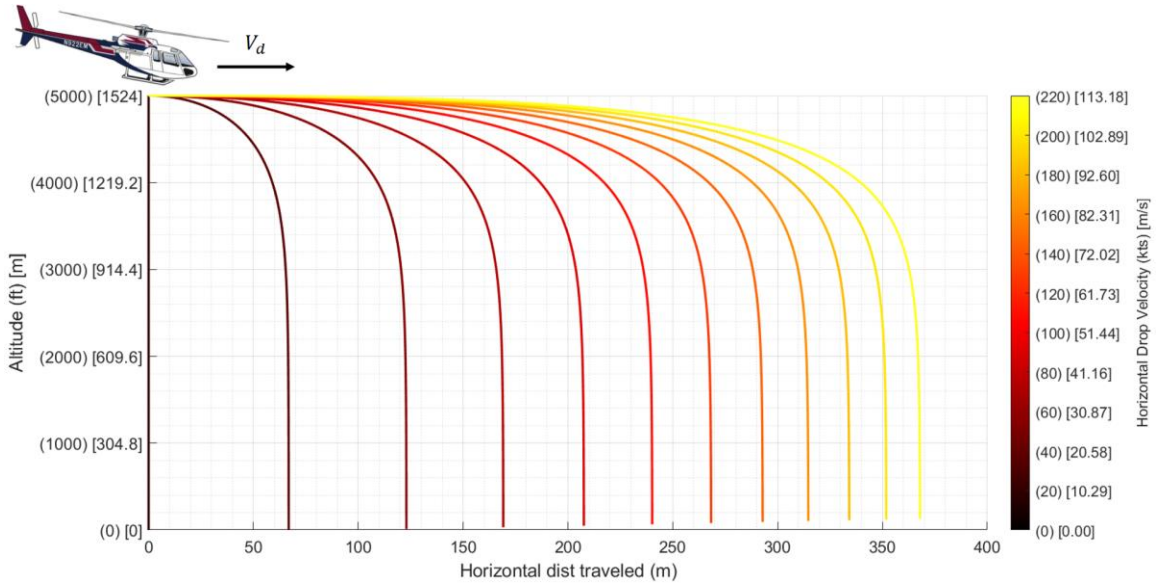


Figure 3-12. Penetrator trajectories w/nonzero drop velocity, zero wind.

Horizontal velocities up to 220 kt are considered, encompassing the full range of possible drop velocities. The world speed record by a true helicopter is held by a modified Westland Lynx AH.1 at 216 kt [17]. Even at 220 kt, a drop from an altitude of 5000 ft will cause the penetrator to cover just under 370 meters horizontally in a zero-wind condition. In the presence of wind, the helicopter should avoid flying with a tailwind if excessive distance travelled by the penetrator is not desired. Figure 3-13 below shows the resulting penetrator trajectories if the helicopter hovers or flies into a 7.5 m/s headwind. The values of V_d indicate the airspeed, not ground speed, of the helicopter.

Interesting to note, if the penetrator is dropped from a helicopter flying at 140 kt into a 7.5 m/s headwind at 5000 ft, the impact point is directly underneath the drop location.

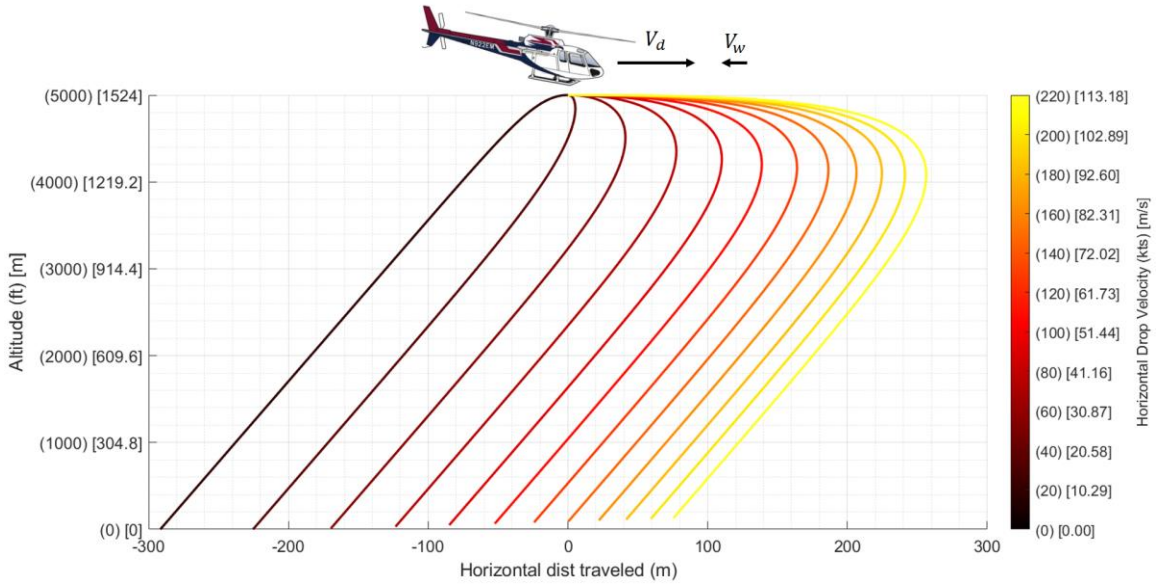


Figure 3-13. Penetrator trajectories w/ helicopter flying into 7.5 m/s headwind.

If the penetrator is dropped from rest, it falls for 1000 ft over a duration of about 10 seconds before reaching terminal velocity. Once at terminal velocity, Table 3-2 indicates that the penetrator will spend about 20 seconds recovering from any pitch perturbation it may encounter. At 42.5 m/s, 20 seconds translates to 850 m, or about 2800 feet of altitude. Adding about 1200 ft of margin, the author recommends a drop altitude of 5000 ft (1524 m) to best ensure vertical emplacement. If dropped from 5000 ft, the flight time of the penetrator is approximately 39 seconds.

4. Impact Simulation

ANSYS Explicit Dynamics is used to simulate the impact event. The Explicit Dynamics module specializes in solving transient, non-linear problems involving high strain rates and significant material deformation [18]. Examples of such problems include drop tests, high velocity and hypervelocity impacts, and explosions.

4.1 Problem Formulation in ANSYS

The first step to building an ANSYS Explicit Dynamics model is to define the geometry to be simulated. The geometry must include snow and ice layers along with a penetrator model. The penetrator in ANSYS consists of two solid bodies – one for the body section and one for the aft flare. No detailed geometry of internal penetrator components is included in order to keep the computational cost manageable. Next, all bodies are assigned material models, a mesh is generated, and the penetrator body and flare are given an initial velocity into the snow pack.

The full three-dimensional geometry is considered only for cases with a horizontal wind-induced velocity component. For all cases involving vertical velocity only, a two-dimensional axisymmetric simulation is run. A detailed overview on setting up the axisymmetric simulation is documented in a YouTube video: https://www.youtube.com/watch?v=doktECLvsJM

ANSYS includes an extensive library cataloging a wide range of material models, but does not provide any information for the behaviors of snow or ice. As such, the first task of setting up the impact simulation is to define the appropriate material models.

4.1.1 Ice Model

Professor Katarina Miljkovic from Curtin University implemented a water ice material model for use in AUTODYN, the solver used by ANSYS Explicit Dynamics, for a study on high velocity impact events onto icy solar system bodies [19]. She graciously shared the details of the ice material model with the author, which are summarized below.

The ice model incorporates a Johnson-Cook strength model with the parameters tabulated in Table 4-1.

Table 4-1. Johnson-Cook strength model for ice [19].

Parameter	Value
Shear modulus	3.6 GPa
Yield strength, A	54 MPa
Strain rate constant, C	0.034

The model also defines a polynomial equation of state with the below parameters. The equation of state is valid for pressures up to 3 GPa, an order of magnitude in excess of the highest pressure seen during the penetrator impact.

Table 4-2. Polynomial EOS for ice [19].

Parameter	Value [GPa]
Bulk modulus, A_1	10
A_2	-50
A_3	50
T_1	10
B_0, B_1, T_2	0

Finally, a material failure model incorporating a principal tensile failure stress and a fracture energy is defined according to Table 4-3.

Table 4-3. Failure model for ice [19].

Parameter	Value
Principal tensile failure stress, T_{max}	8 MPa
Fracture energy, G_c	15 J m^{-2}

4.1.2 Snow Model

Snow is somewhat complicated to model since its properties depend so heavily on density. Snow density can vary from 200 kg/m^3 if freshly deposited to over 800 kg/m^3 if sufficiently compacted, at which density it starts to lose its porosity and more closely resembles ice than snow [20]. Several properties vary by over an order of magnitude across the density range of snow, but these properties are well defined for any given snow density. Thus, all snow properties are commonly described as functions of density, and density is used to fully define the snow state [20].

Mellor finds the relationship between overburden pressure and snow depth closely described by

$$P = 3750d \qquad 4\text{-}1$$

for shallow depths, as shown in Figure 4-1. Here, the pressure P is given in Pa and depth d is given in meters.

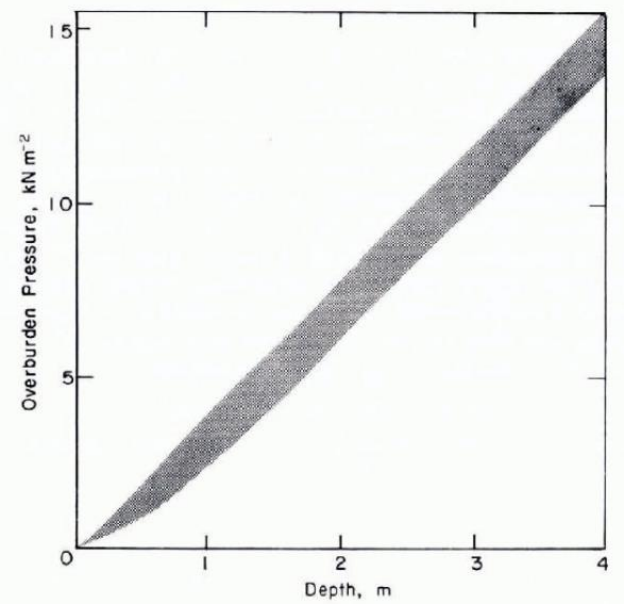


Figure 4-1. Snow overburden pressure vs depth [20].

The same study also catalogues the relationship between depth and snow density, enabling one to describe the variability of snow density with pressure. No explicit equation is given to relate density directly to depth, so average density values were manually read for a range of depths from Figure 4-2. The depth values are converted to pressure via equation 4-1, yielding a data set describing snow density as a function of pressure.

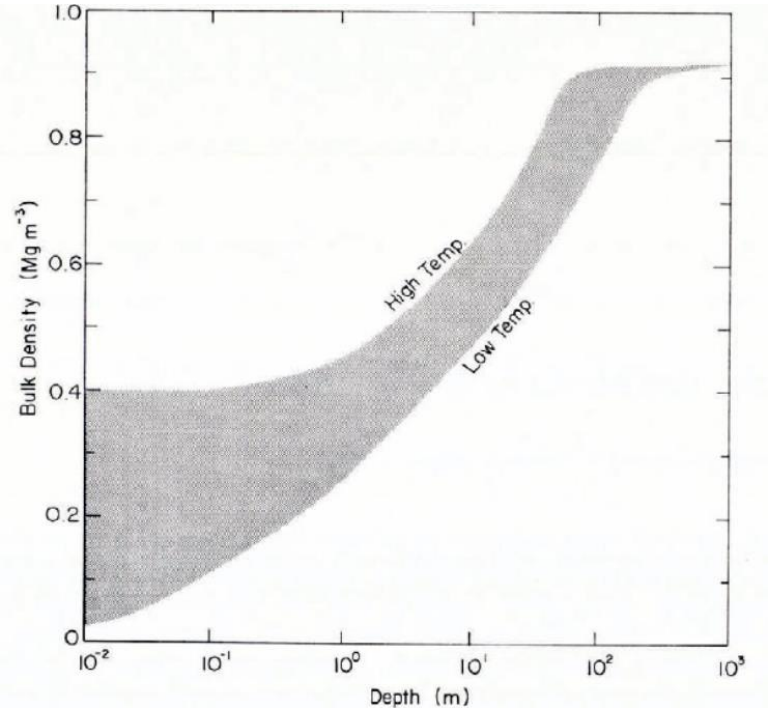


Figure 4-2. Snow density vs depth [20].

Van Herwijnen et al. describe a power law relationship between snow density and elastic modulus given by

$$E = 0.93\rho^{2.8} \qquad 4\text{-}2$$

where E has units of Pa and ρ has units of kg/m^3 [21]. The power law fit is shown as the blue dashed line overlaying field data in Figure 4-3.

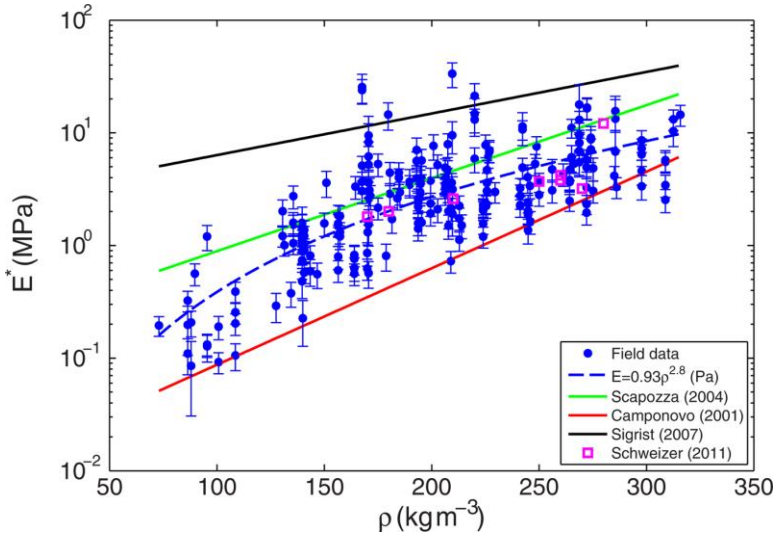


Figure 4-3. Snow elastic modulus vs density [21].

Since ANSYS asks for stiffness in the form of shear modulus instead of elastic modulus, the latter is converted to the former via

$$G = \frac{E}{2(1+\nu)} \tag{4-3}$$

where ν is Poisson's ratio. According to Shapiro et al., the Poisson's ratio stays approximately constant at a value of around 0.3 throughout the full density profile of snow [22].

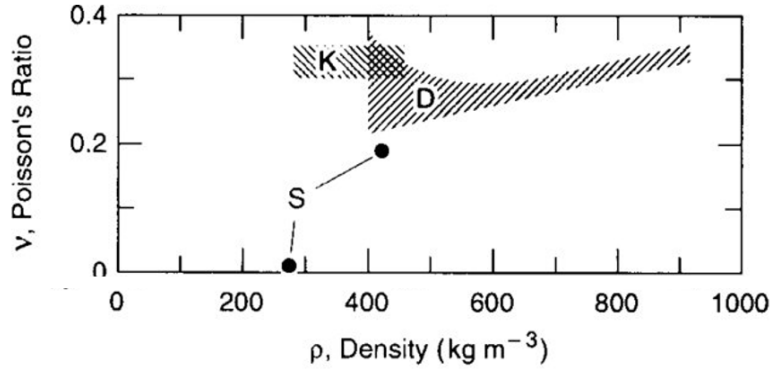


Figure 4-4. Poisson's ratio of snow vs density [22].

Sommerfeld relates the tensile strength of snow to density according to

$$\log_{10}\sigma_m = -4.3 + 3\log_{10}\rho \tag{4-4}$$

where σ_m has units of 10^2 Pa and ρ has units of kg/m³ [23]. The log-log relationship is overlaid on field data below in Figure 4-5.

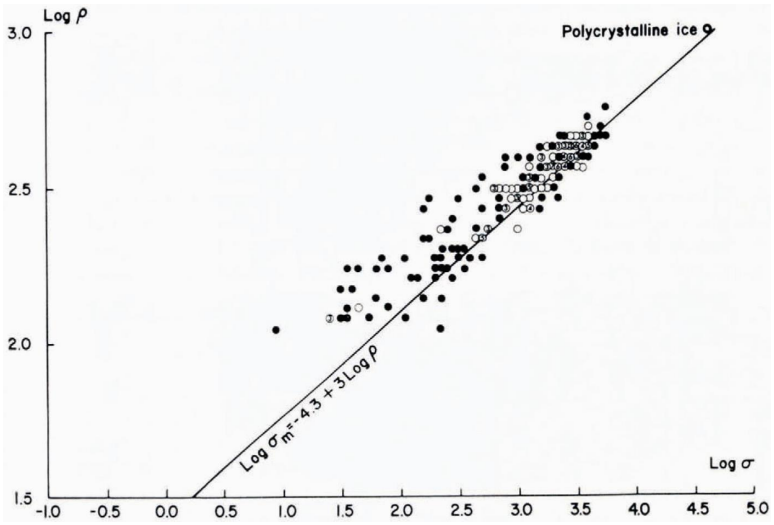


Figure 4-5. Log density vs log tensile strength of snow [23].

The relationships found above are valid for snow densities up to approximately 850 kg/m^3, past which point the snow morphs into ice. Thus, the properties of snow jump to those of ice once the density exceeds 850 kg/m^3. The snow properties found above are shown in Figure 4-6 along with the transition to ice. The transition is also visible in Figure 4-2.

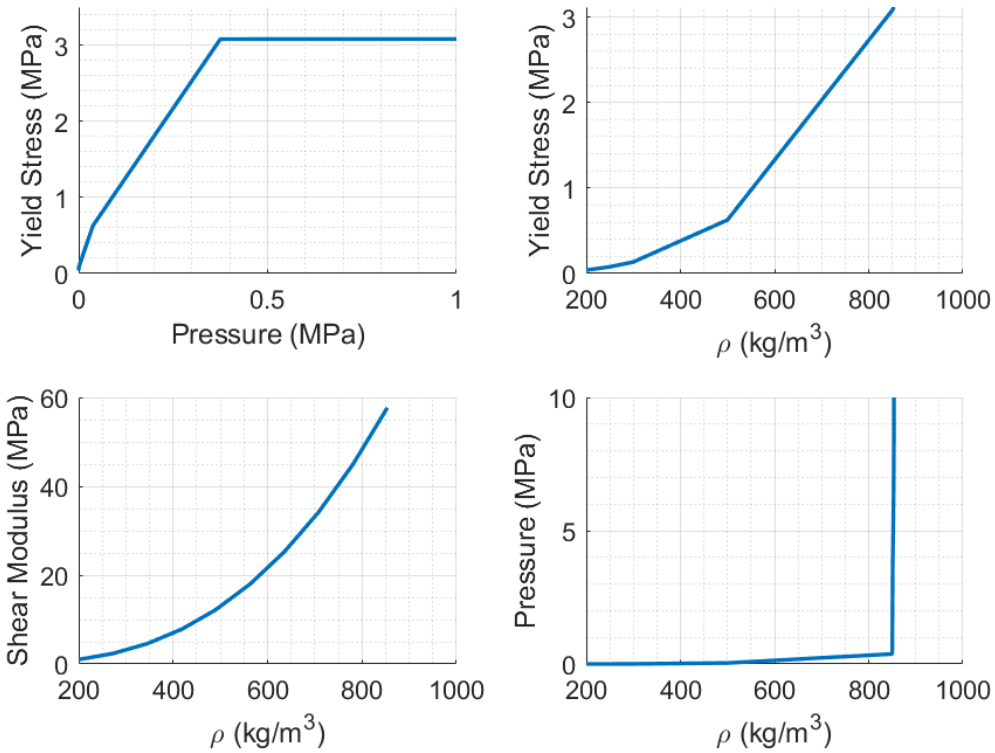


Figure 4-6. Snow yield stress, pressure, shear modulus, and density.

The relationships between yield stress and pressure, yield stress and density, and shear modulus and density shown in Figure 4-6 are implemented into an MO Granular model in ANSYS.

The speed of sound is another important parameter affecting the compaction of snow, and experimental results have been found to vary wildly. Capelli et al. documented the results of a number of studies in 2016 [24]. Their own results are also shown and are marked "present study" in Figure 4-7. For the purposes of this research, the speed of sound is taken as fitting the middle set of data in Figure 4-7, i. e. fitting the results of Smith 1965 transversal, Smith 1965 Rayleigh, Yamada et al. 1974 transversal, Takei and Maeno 2004 Transversal, and Capelli et al. 2016 (marked "present study").

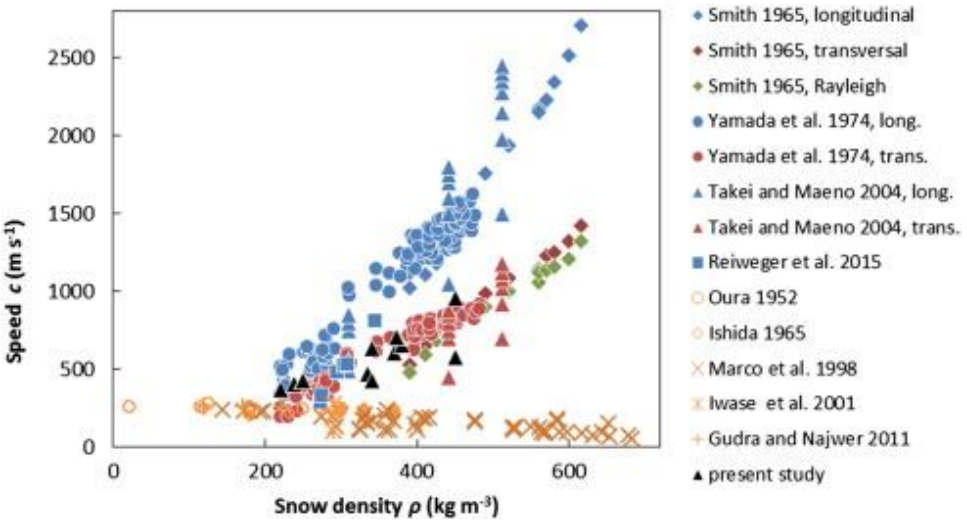


Figure 4-7. Speed of sound through snow vs density [24].

A compaction equation of state model is defined in ANSYS using the pressure/density relationship of snow. Pressures up to 10^8 Pa are considered, above which point regelation, i. e. pressure-induced melting, will start to play a role at a temperature of around -10°C [25]. Additionally, the compaction EOS takes in data for the speed of sound as a function of density.
Camponovo and Schweizer find snow grains to fail at a strain of about 0.35 [26], a value implemented into a strain failure model in ANSYS.

Finally, a crack softening failure model is also defined for snow. Van Herwijnen et al. find the fracture energy of snow to vary anywhere from 0.08 J/m² to 2.7 J/m² [21], but unfortunately, ANSYS does not allow for a variable fracture energy. Since a constant number must be input, a mid-range value of 1.4 J/m² is chosen.

4.1.3 Penetrator Material Models

Since the body and flare are both modeled as solid bodies in ANSYS, their densities must be adjusted to yield realistic mass values. Table 4-4 below shows the mass, volume, and required density of the body and flare ANSYS models.

Table 4-4. Mass, volume, and density of penetrator ANSYS model.

Parameter	Body	Flare
Mass (kg)	66.62	25.58
Volume (m^3)	0.0682	0.2115
Density (kg/m^3)	976.7	120.9

For rigidity, the body and flare are both assigned 304 stainless steel as their material. The densities are overridden with the appropriate values from Table 4-4.

4.2 Speed Study

The Explicit Dynamics module in ANSYS is used to simulate a 2D axisymmetric penetrator impact into a snow/ice assembly at velocities of 20, 30, 40, and 50 m/s. The assembly includes a two-piece penetrator, various snow and ice layers, and a hard wall to enforce boundary conditions. The penetrator is comprised of a flare and body section with no mechanical connection to each other. They are specified to move downward with matching initial velocities and separate as soon as the flare contacts the snow/ice surface.

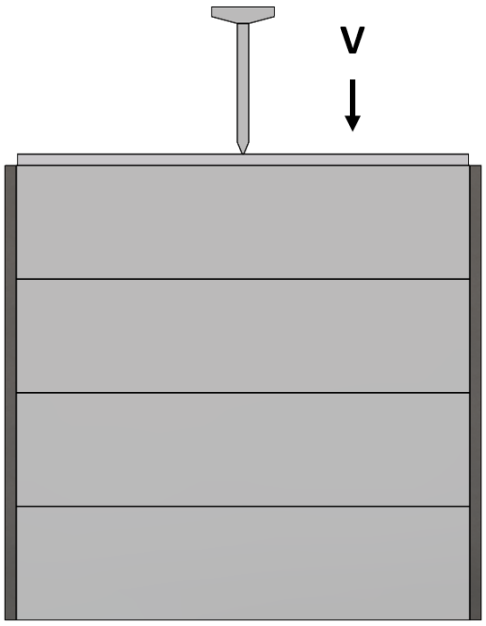


Figure 4-8. CAD model of impact assembly for speed study.

The geometry used for the speed study includes four 2 m thick snow layers with respective densities of 440, 480, 520, and 560 kg/m^3. The increasing density simulates the compressive effects of overburden pressure, the solid material-equivalent of hydrostatic pressure in a liquid. A 10 cm thick ice layer rests on the surface. For analysis of an impact into a pure snow pack with no ice layer, the material of the thin layer is also set to snow of density 440 kg/m^3.
The density values are chosen to match the density profile of snow in Marie Byrd Land, just east of the Ross Ice Shelf, as found by Ligtenberg et al. in 2011 [27].

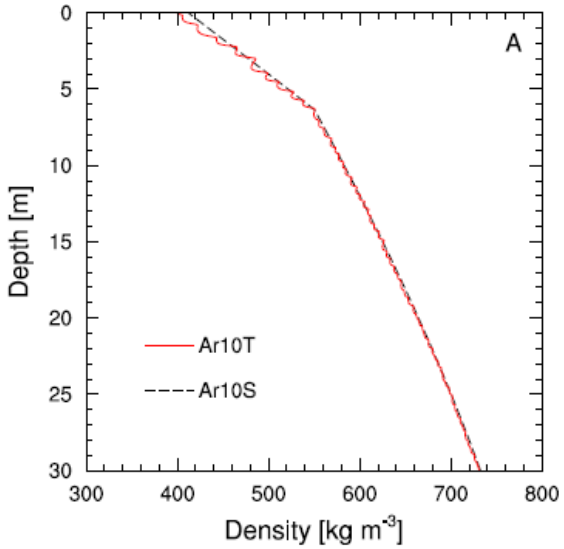


Figure 4-9. Density profile of snow in Marie Byrd Land [27].

Since ANSYS Explicit Dynamics does not support frictionless boundary conditions but does support frictionless contact between surfaces, the inner surface of the hard wall is defined to be in frictionless contact with the snow and ice layers. The external surface of the hard wall and bottom surface of the lowest snow layer are fixed.

Results for the 10 cm ice layer are shown below in Figure 4-10 to Figure 4-13:

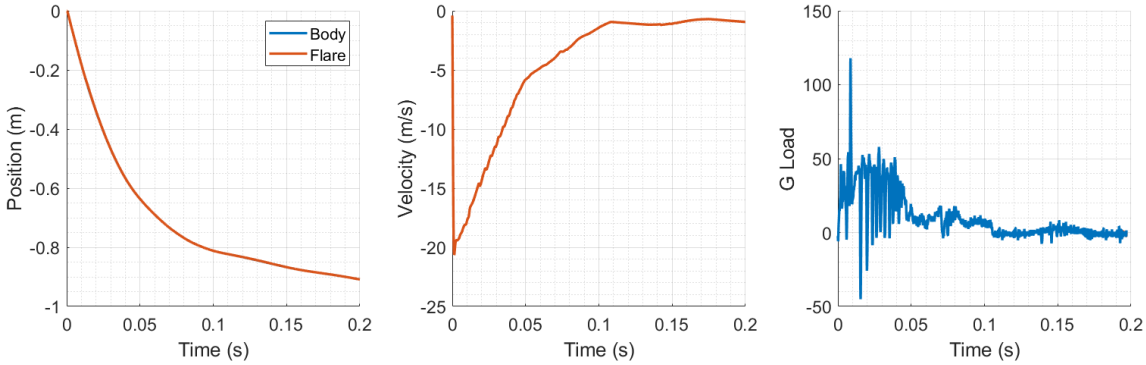


Figure 4-10. Vertical position, velocity, and G load for $V = 20\frac{m}{s}$, 10 cm ice layer.

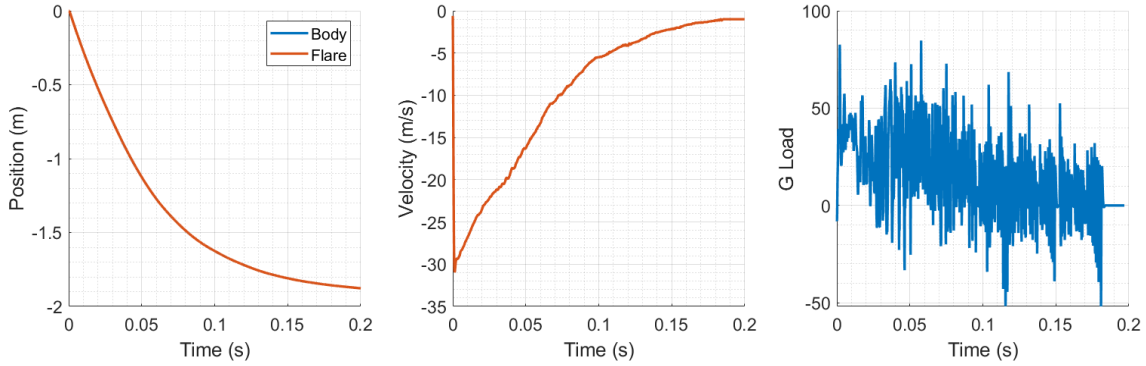


Figure 4-11. Vertical position, velocity, and G load for $V = 30\frac{m}{s}$, 10 cm ice layer.

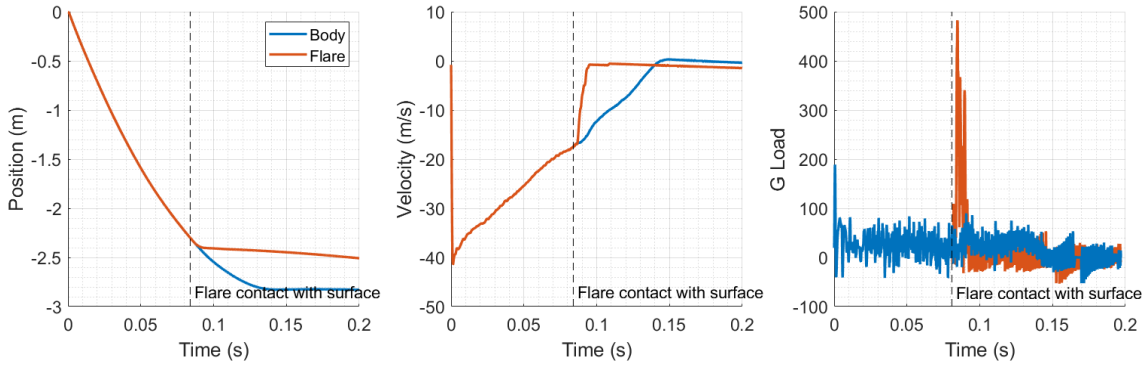


Figure 4-12. Vertical position, velocity, and G load for $V = 40\frac{m}{s}$, 10 cm ice layer.

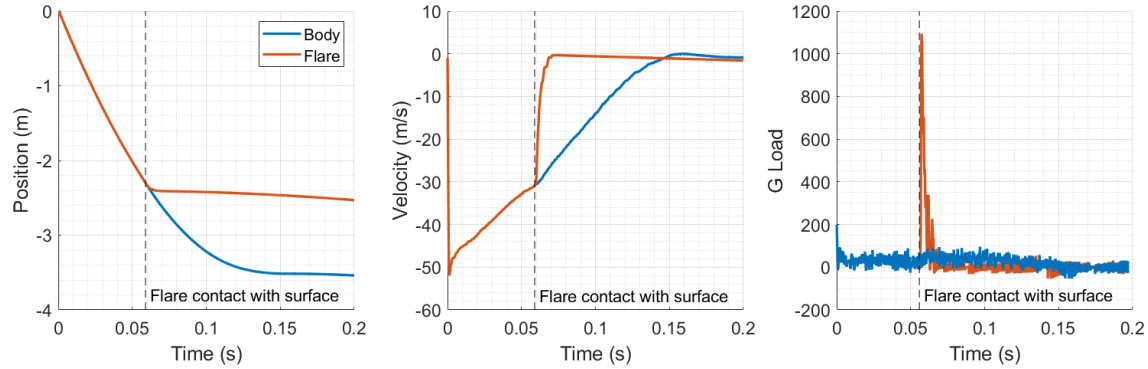


Figure 4-13. Vertical position, velocity, and G load for $V = 50\frac{m}{s}$, 10 cm ice layer.

Results for no ice layer are shown below in Figure 4-14 to Figure 4-17:

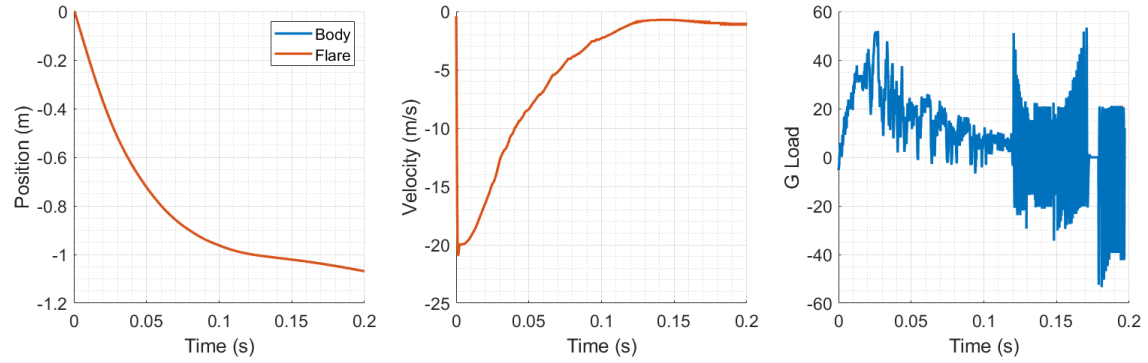


Figure 4-14. Vertical position, velocity, and G load for $V = 20\frac{m}{s}$, no ice.

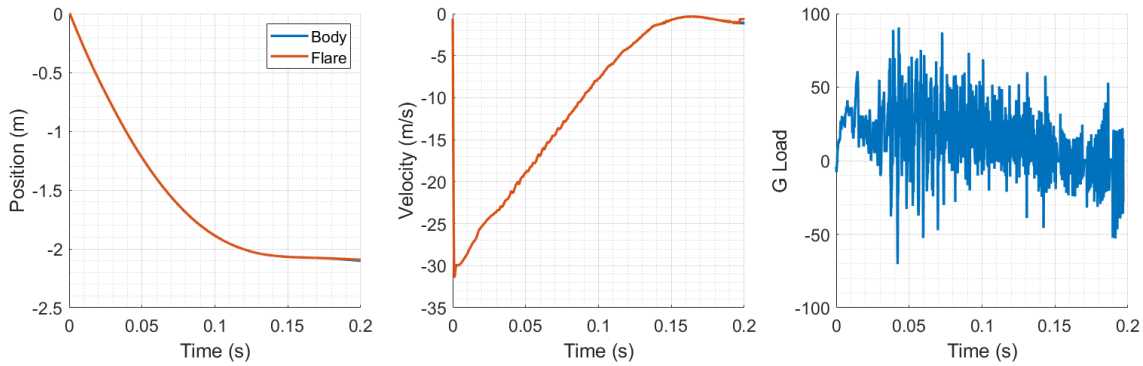


Figure 4-15. Vertical position, velocity, and G load for $V = 30\frac{m}{s}$, no ice.

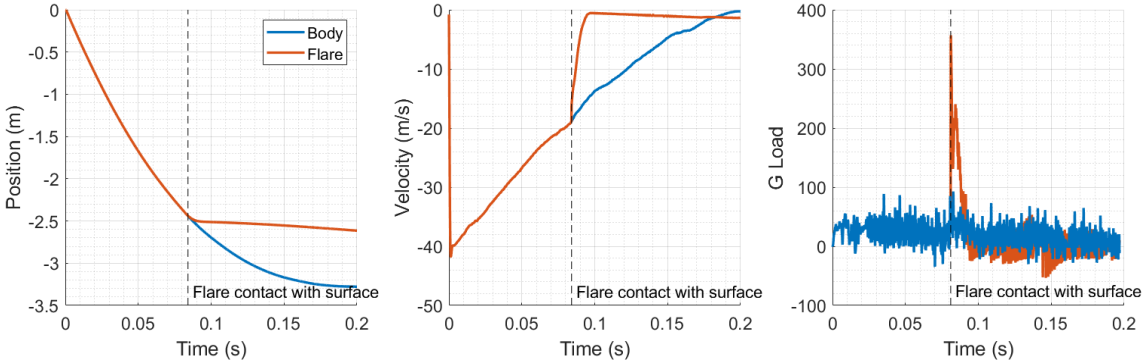


Figure 4-16. Vertical position, velocity, and G load for $V = 40\frac{m}{s}$, no ice.

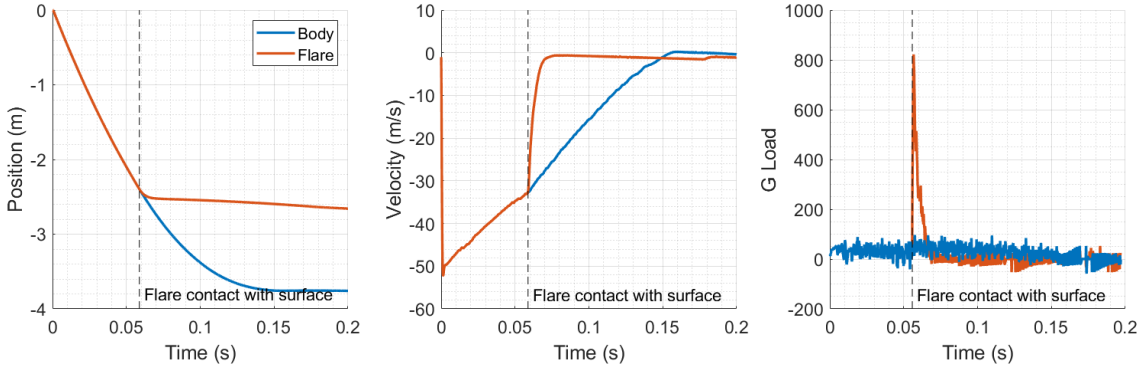


Figure 4-17. Vertical position, velocity, and G load for $V = 50\frac{m}{s}$, no ice.

Table 4-5. Final depth, flare impact velocity, and max G load for 10 cm ice layer.

Initial velocity (m/s)	Final penetrator depth (m)	Flare velocity at surface impact (m/s)	Max flare G load
20	0.91	N/A	117.9
30	1.88	N/A	84.7
40	2.83	17.42	482.6
50	3.54	30.70	1094.3

Table 4-6. Final depth, flare impact velocity, and max G load for no ice layer.

Initial velocity (m/s)	Final penetrator depth (m)	Flare velocity at surface impact (m/s)	Max flare G load
20	1.07	N/A	53.4
30	2.10	N/A	90.6
40	3.28	16.21	357.1
50	3.76	32.55	822.2

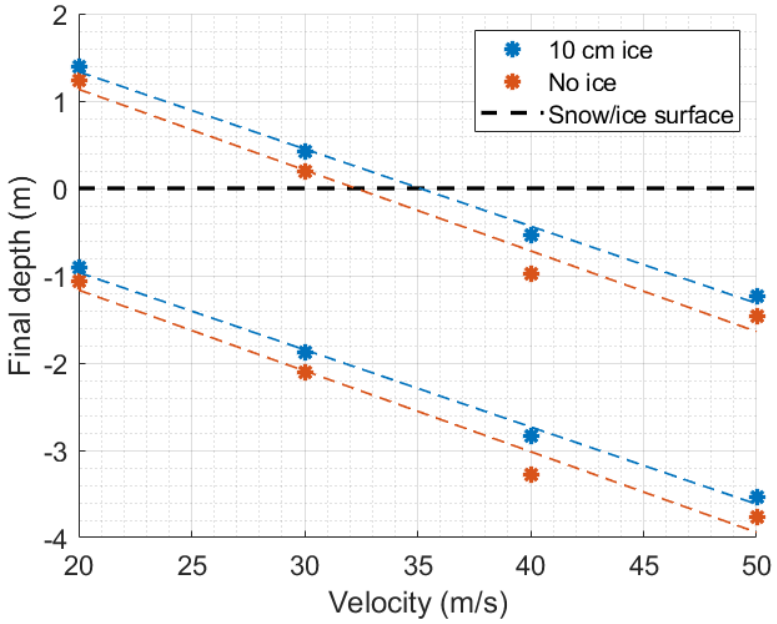


Figure 4-18. Final resting depth of penetrator as function of drop velocity.

The lower set of data in Figure 4-18 corresponds to the final resting position of the penetrator nose. For reference, the final resting position of the aft end of the penetrator body is shown above the lower data set, allowing for easy determination of whether or not the penetrator body fully embeds itself into the snow pack at any given velocity. The data unanimously indicate that the penetrator burrows deeper in the absence of ice, suggesting that breaking through the ice layer depletes some of the penetrator's kinetic energy. On average, the penetrator comes to rest 26.25 cm deeper in the no ice case as compared to the 10 cm ice layer case.

Penetration depth appears to follow a roughly linear relationship with drop velocity. With a 10 cm ice layer, the linear fit of penetration depth of the nose is given by

$$d_{10} = -0.0884V_T + 0.8040 \qquad 4\text{-}5$$

where d_{10} is the penetration depth in meters and V_T is the terminal velocity of the penetrator in meters per second. Since the penetrator body length is 2.299 meters, the minimum required velocity for full penetration into the snow pack is 35.15 m/s.

Similarly, the linear fit of nose penetration depth with no ice is given by

$$d_0 = -0.0925V_T + 0.6850 \qquad 4\text{-}6$$

Again, d_0 is the penetration depth in meters and V_T is the terminal velocity in m/s. For the case with no ice, the minimum required velocity for full penetration is 32.27 m/s.

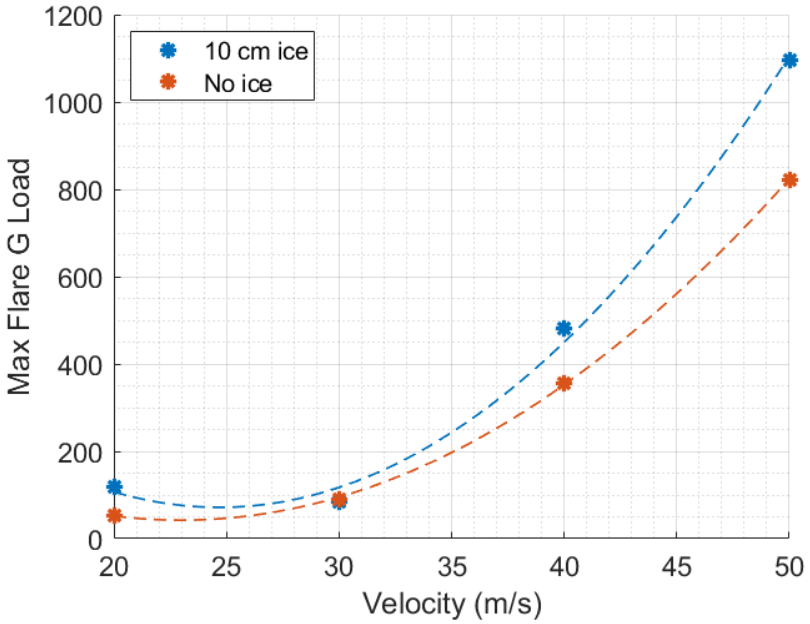


Figure 4-19. Max G load on flare as function of drop velocity.

The maximum acceleration experienced by the flare seems to be well described by a quadratic function for drop velocities ranging from 20 to 50 m/s. For the 10 cm ice layer case, the quadratic fit is given by

$$G_{10} = 1.612V_T^2 - 79.59V_T + 1054.0 \qquad 4\text{-}7$$

while for the 0 cm ice layer case, it is given by

$$G_0 = 1.070V_T^2 - 49.15V_T + 607.0 \qquad 4\text{-}8$$

In both cases, G_i is the maximum acceleration felt by the flare upon impact in units of $\frac{m/s^2}{9.8066\ m/s^2}$.

4.3 Depth Study

For the depth study, ANSYS Explicit Dynamics is used to simulate a 2D axisymmetric penetrator impact into a snow/ice assembly of varying geometry at a velocity of 42.5 m/s. Again, the assembly includes a two-piece penetrator, various snow and ice layers, and a hard wall to enforce boundary conditions. The penetrator is comprised of a flare and body section with no mechanical connection to each other. They are specified to move downward with matching initial velocities and separate as soon as the flare contacts the snow/ice surface.

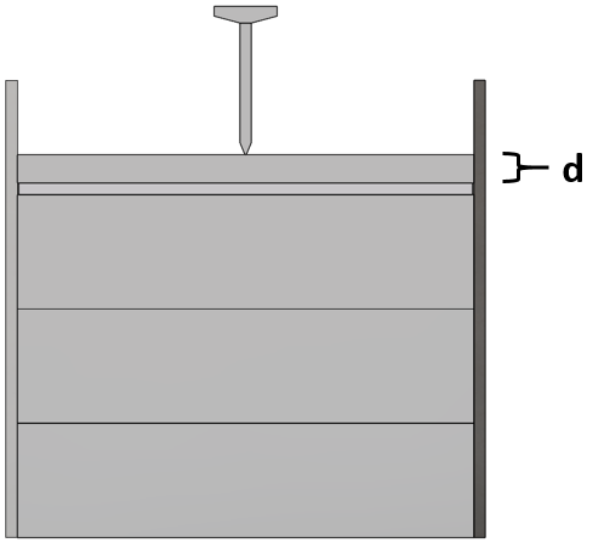


Figure 4-20. CAD model of impact assembly for depth study.

In Figure 4-20, the parameter d represents the depth at which the ice layer resides. Simulations were run for values of d of 0.5, 1, 1.5, and 2 meters with ice layer thicknesses of 10 and 20 cm.

Results for the 10 cm thick ice layer are shown below.

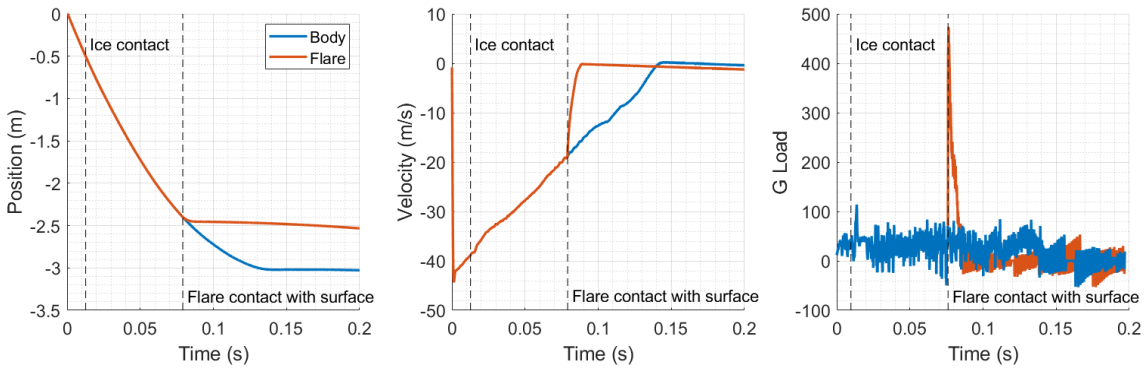


Figure 4-21. Vertical position, velocity, and G load for $d = 0.5\,m$, 10 cm ice layer.

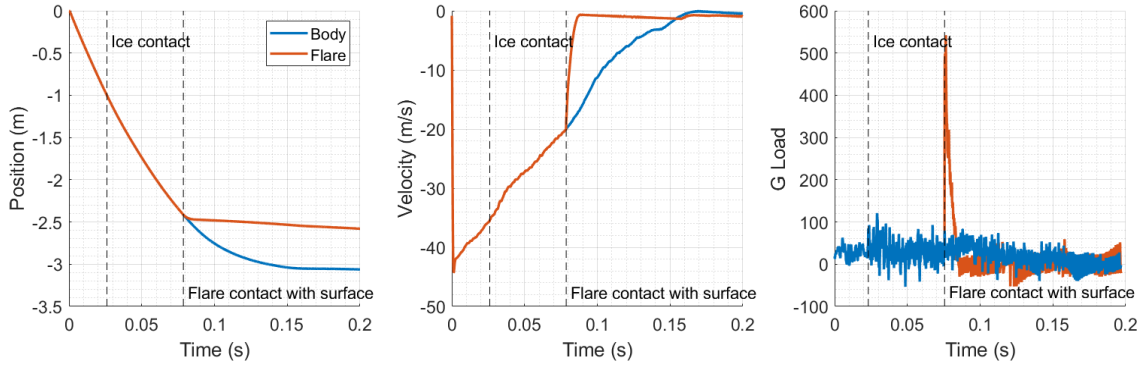


Figure 4-22. Vertical position, velocity, and G load for $d = 1\,m$, 10 cm ice layer.

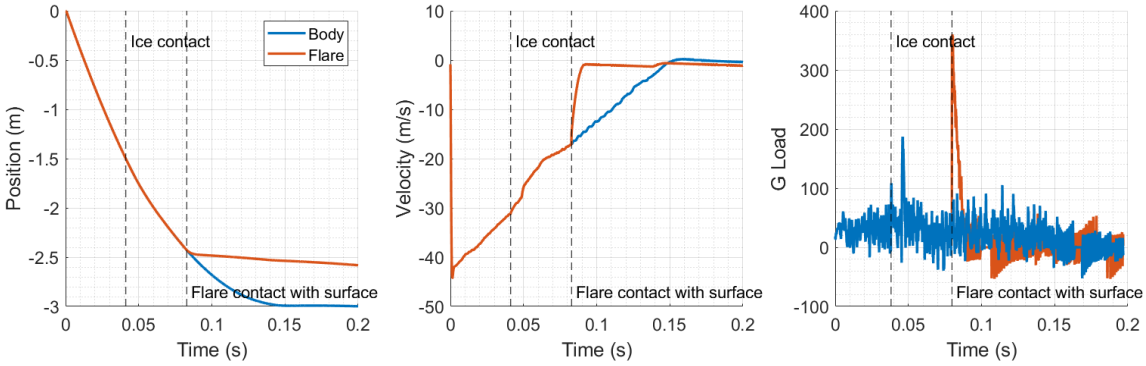


Figure 4-23. Vertical position, velocity, and G load for $d = 1.5\,m$, 10 cm ice layer.

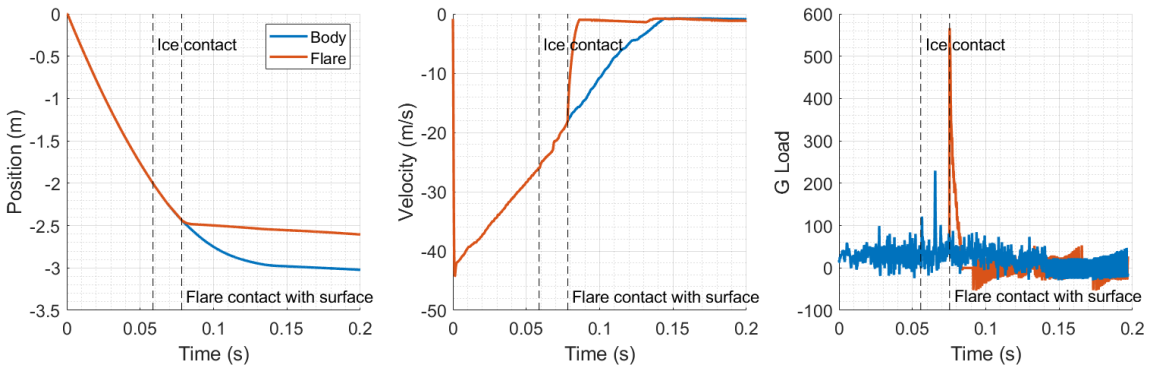


Figure 4-24. Vertical position, velocity, and G load for $d = 2\,m$, 10 cm ice layer.

Although the maximum body deceleration exceeds the seismometer's 100 G limit in some cases, the duration of said maximum is fleeting. The seismometer is rated to a half-sine with a 100 G peak and a duration of 5 ms, representing significantly higher impact energy than any of the body acceleration spikes above 100 G in Figure 4-21 to Figure 4-24.

Results for the 20 cm thick ice layer are shown below.

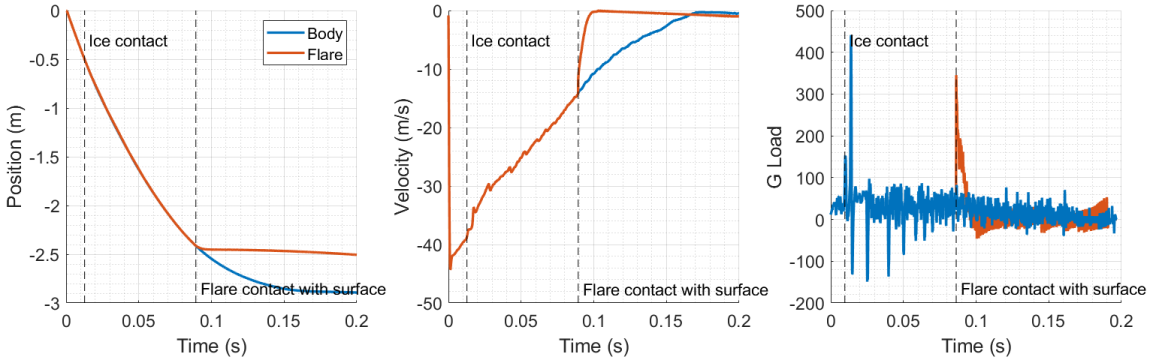


Figure 4-25. Vertical position, velocity, and G load for $d = 0.5\,m$, 20 cm ice layer.

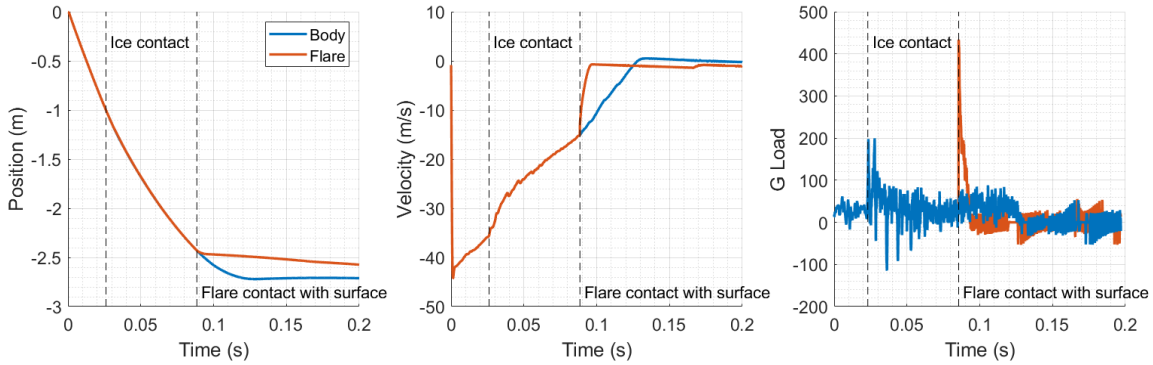


Figure 4-26. Vertical position, velocity, and G load for $d = 1\,m$, 20 cm ice layer.

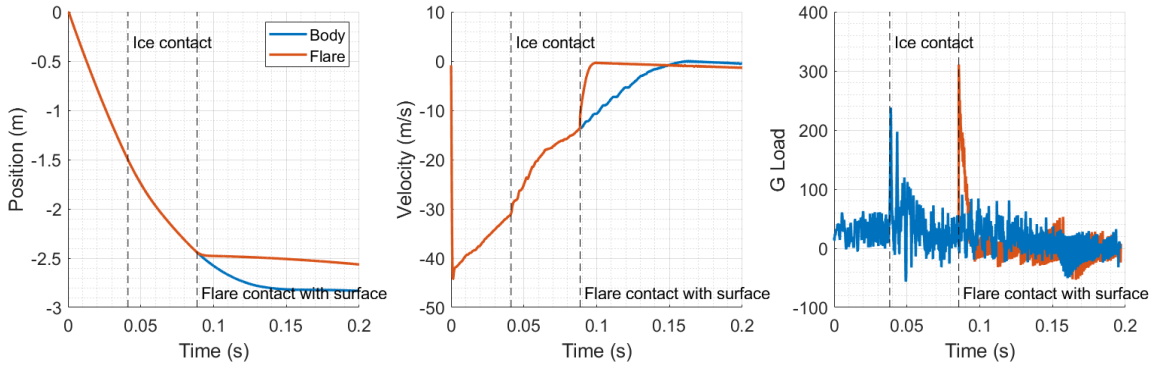


Figure 4-27. Vertical position, velocity, and G load for $d = 1.5\,m$, 20 cm ice layer.

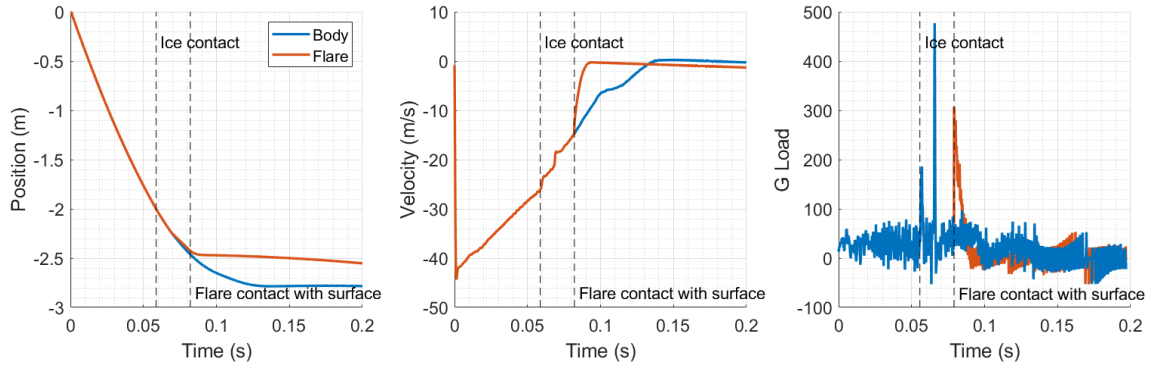


Figure 4-28. Vertical position, velocity, and G load for $d = 2\,m$, 20 cm ice layer.

A noticeable increase in G load is visible in all cases when the nosecone breaks through the ice layer. The leftmost vertical dashed line in Figure 4-21 to Figure 4-28 corresponds to the tip of the nosecone making initial contact with the submerged ice layer. In many cases, such as that illustrated in Figure 4-28, the highest G load felt by the body does not occur exactly at the initial contact with

ice. Rather, it occurs on the order of 10 milliseconds later, when the widest section of the nosecone impacts the ice layer. The maximum acceleration felt by the body exceeds the seismometer's 100 G limit in all cases with a 20 cm ice layer. Before executing a drop operation, the author recommends sparing no expense to determine whether or not 20+ cm thick ice layers are actually present in the top 3 meters of the Ross Ice Shelf snow pack. The depth study results are summarized in Table 4-7 and Table 4-8 below.

Table 4-7. Final depth, flare impact velocity, and max G load for 10 cm ice layer.

Ice layer depth (m)	Final penetrator depth (m)	Flare velocity at surface impact (m/s)	Max flare G load
0.5	3.03	17.34	473.8
1	3.06	18.78	541.3
1.5	3.00	14.87	360.2
2	3.02	16.67	566.4

Table 4-8. Final depth, flare impact velocity, and max G load for 20 cm ice layer.

Ice layer depth (m)	Final penetrator depth (m)	Flare velocity at surface impact (m/s)	Max flare G load
0.5	2.89	11.58	441.4 (B)
1	2.72	12.88	433.6
1.5	2.83	11.22	310.8
2	2.79	12.56	476.9 (B)

The (B) suffixes in the last column of Table 4-8 indicate that the maximum G load felt by the flare is equal to the maximum G load felt by the body – that is, it occurs at ice impact before the flare and body have separated. Regardless of whether the maximum G load occurs at ice impact or flare impact, for any given depth, the maximum G load is always higher for a 10 cm ice layer than a 20 cm layer.

The faster flare velocities at impact for the 10 cm ice layer offer a physical explanation for the higher G loading. The average flare velocity at impact for a 10 cm ice layer is 16.91 m/s as compared to 12.06 m/s for a 20 cm ice layer. Assuming a penetrator mass of 92 kg, the average velocity difference indicates that the penetrator spends an additional 6.46 kJ of kinetic energy puncturing the thicker 20 cm ice layer as compared to the 10 cm layer. To provide further insight into the relationship between flare velocity at impact and maximum G load felt by the flare, Figure 4-29 below shows the latter as a function of the former. The six blue data points are those from Table 4-7 and Table 4-8 where the maximum G load is felt upon flare impact. The two data points marked (B) are not shown.

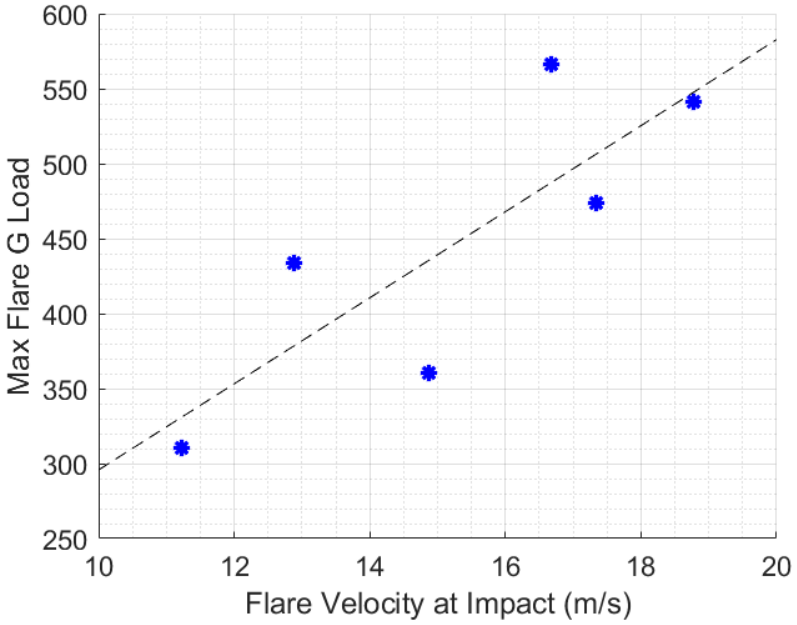


Figure 4-29. Max flare G load vs flare velocity at impact.

A clear upward trend is visible in Figure 4-29. The linear fit shown is given by

$$G = 28.70V_F + 8.81 \qquad 4\text{-}9$$

where G is the maximum G load on the flare and V_F is the flare velocity at impact in m/s.

The rest of the data from Table 4-7 and Table 4-8 are visualized in Figure 4-30 and Figure 4-31 below.

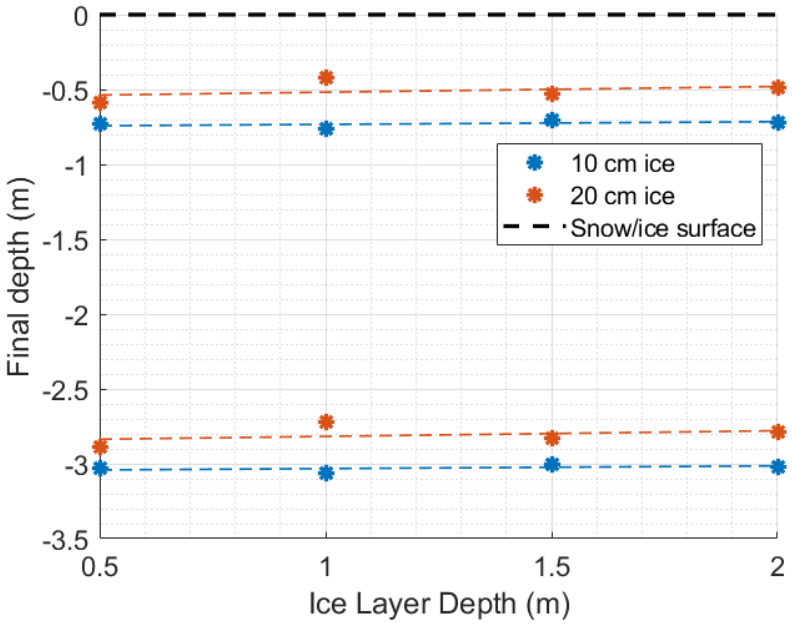


Figure 4-30. Final resting depth of penetrator as function of ice layer depth.

The maximum penetration depth is independent of the ice layer depth, but does vary with ice layer thickness. The average final resting depth of the tip of the nosecone is 3.03 m for a 10 cm ice layer and 2.81 m for a 20 cm layer. Again, the upper and lower data sets in Figure 4-30 only differ by a fixed 2.299 meters, the length of the penetrator body. The lower data set shows the resting depth of the tip of the nosecone, while the upper set shows the resting depth of the aft end of the penetrator body.

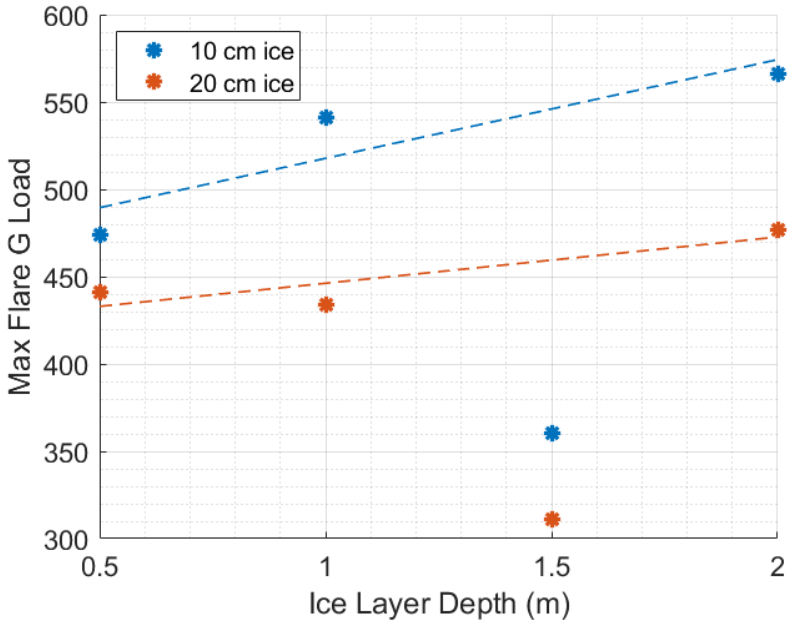


Figure 4-31. Max G load on flare as function of ice layer depth.

Figure 4-31 does not show as clear-cut of a relationship as Figure 4-19 does. One influencing factor may be that the flare impacting the snow surface is not always the event that produces the maximum G loading, as indicated in Table 4-8. A 20 cm thick ice layer at a depth of 0.5 or 2 meters will produce a higher G loading when the nosecone passes through it than when the flare impacts the surface. Disregarding the outlying low G load values at an ice layer depth of 1.5 m, a somewhat conservative estimate can be made for the maximum G load experienced by the flare. Linear fits are shown for both the 10 cm and 20 cm ice layer cases in Figure 4-31. Both fits exhibit a weak upward trend with increasing ice layer depth, although neither fit can be claimed conclusive since both are based on only three data points. Equations for the linear fits are given below:

$$G_{10} = 56.50d + 461.25 \qquad 4\text{-}10$$

$$G_{20} = 26.47d + 419.75 \qquad 4\text{-}11$$

Here, G_{10} is the maximum G loading for a 10 cm thick ice layer, G_{20} is the maximum G loading for a 20 cm thick ice layer. and d is the ice layer depth. Both linear fits serve illustrative roles at best, so readers are cautioned not to treat them as indisputable fact.

4.4 Wind-Induced Horizontal Velocity

Assuming steady wind, previous analysis shows that the penetrator will be oriented vertically upon initial contact with the snow pack, regardless of wind velocity. Furthermore, the horizontal velocity will exactly match the wind velocity given a drop altitude of at least 3000 ft (914 m). Thus, the state of the penetrator at the start of impact is fully defined as having its vertical velocity equal to terminal velocity and horizontal velocity equal to the wind speed, with an attitude of zero degrees of tilt as measured from the vertical.

4.4.1 Helicopter Wind Speed Limitation

Air Center Helicopters holds the current contract for helicopter operations based out of McMurdo Station, where they operate two Airbus AS350-B3e A-stars and two Bell 412s [28]. Of the two helicopters, the penetrator will likely be flown on the smaller A-star given its relatively low mass of less than 100 kg. The payload and range capabilities of both helicopters are shown in Figure 4-32.

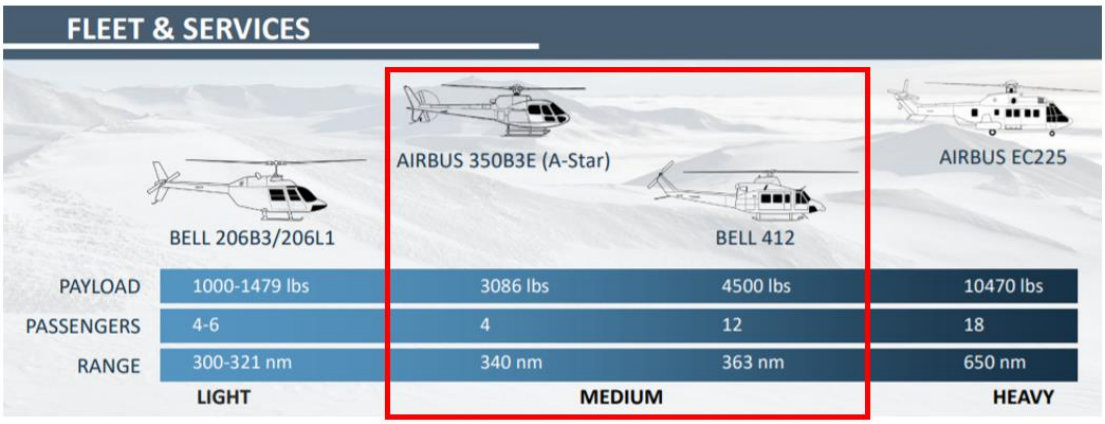


Figure 4-32. Payload and range capabilities of AS350-B3e and Bell 412 [29].

The maximum wind speed that the A-star is rated for everywhere in its flight envelope is 17 kt, or about 8.75 m/s [30]. For comparison, the Bell 412 can tolerate winds of 35 kt or 18 m/s at sea level, falling to 20 kt or 10.3 m/s at 12,000 ft [31].

Wind envelope in hover

Hovering with wind from any direction has been substantiated over the entire flight envelope up to winds of 17 kts, although this is not to be taken as a limit. For example hover at sea level at maximum weight, for all c.g. locations, has been substantiated at 30 knots.

Figure 4-33. Wind rating of AS350-B3e in hover [30].

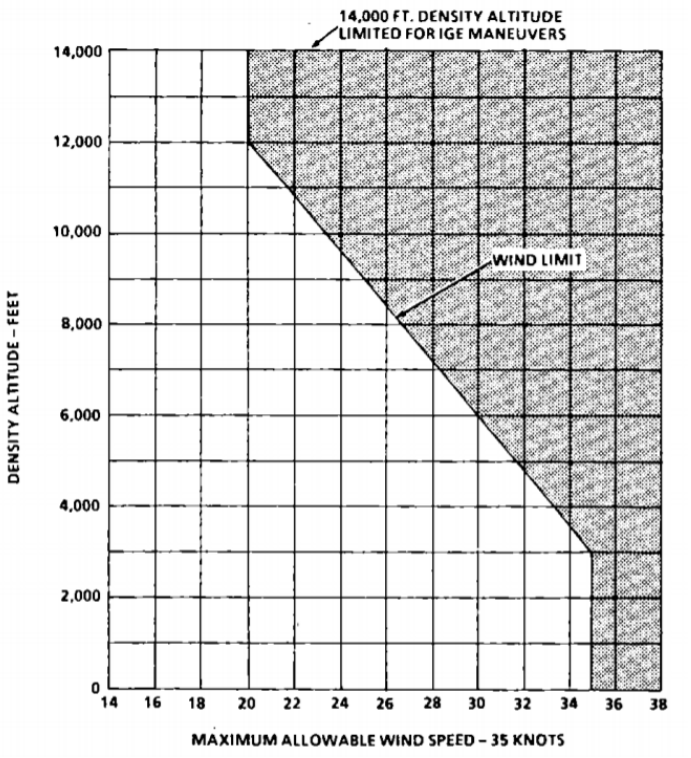


Figure 4-34. Wind rating of Bell 412 in hover [31].

4.4.2. Horizontal Velocity Impact Study

The final analysis conducted as part of this research is aimed to answer the question of how much wind can the penetrator tolerate without tipping over on impact. The vertical velocity of 42.5 m/s remains unchanged, but the horizontal velocity corresponding to possible wind speeds is varied from 2.5 to 30 m/s.

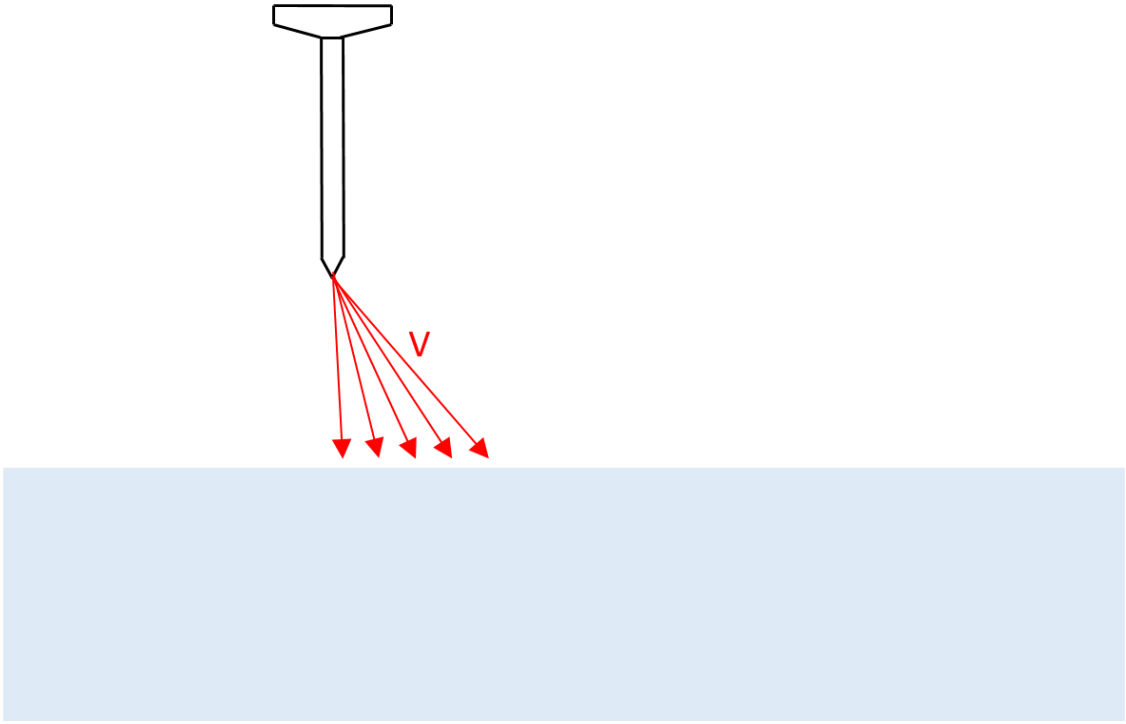


Figure 4-35. Schematic of range of velocities considered for tipping study.

Since the axisymmetric assumption can no longer be made, the problem necessarily becomes more complex. The most accurate model will incorporate the full three-dimensional geometry at the cost of higher computational time. Some simplifying assumptions may be made to attempt to reduce the problem to a two-dimensional planar case, but special care must be taken to ensure maximum physical accuracy. First, the densities of the penetrator body and flare must be proportioned correctly relative to each other so that the mass distribution of the penetrator remains accurate. Second, the penetrator and snow pack densities must also be proportioned to best reflect reality.

The body and flare cannot be defined as two uncoupled bodies for the tipping study because the flare mass contributes to the tipping action of the penetrator. Hence, the flare and body have a bonded connection in the three-dimensional ANSYS model. Since ANSYS Explicit Dynamics does not support bonded contact in its two-dimensional solver, a new CAD model is created where the entire penetrator is one solid part. The single part encompassing the body and flare has uniform density, so the size of the flare must be redefined for the two-dimensional case. The smaller flare is visible and can be compared to the three-dimensional geometry in Figure 4-36. Both models incorporate a thin surface layer on top of the snow pack whose material can be set to either snow or ice.

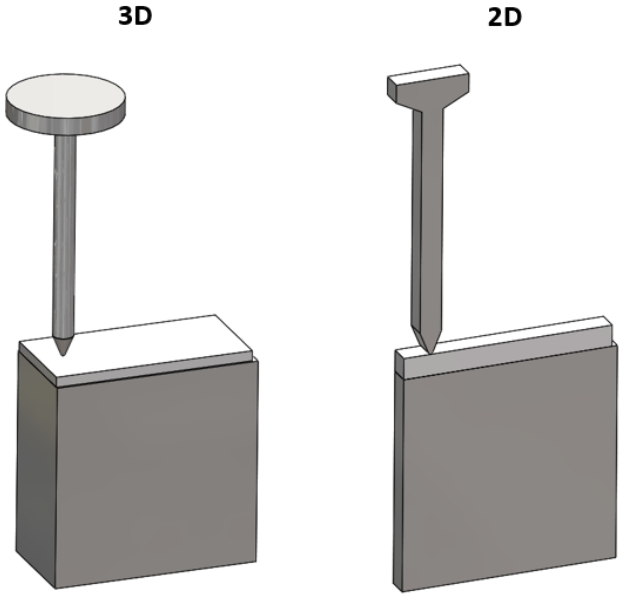


Figure 4-36. 3D and 2D geometries considered for tipping study.

The 20 cm thickness of the two-dimensional model in Figure 4-36 is illustrative only since the analysis uses a cross section of the CAD model. However, considering a 20 cm wide section does have some physical significance since the true penetrator body diameter is 20 cm. With any horizontal velocity, the three-dimensional cylindrical body will plow a 20 cm wide swath through the snow as it penetrates. Therefore, the total mass of a 20 cm wide section of the two-dimensional penetrator should match that of the three-dimensional penetrator. Table 4-9 below shows the scaling required to model an accurate mass distribution in the two-dimensional model.

Table 4-9. 2D mass and volume scaling for tipping study.

Parameter	3D	2D (per 20 cm thickness)
Body mass (kg)	66.62	66.62
Flare mass (kg)	25.58	25.58
Body density (kg/m^3)	976.7	754.0
Flare density (kg/m^3)	120.9	754.0
Body volume (m^3)	0.0682	0.0884
Flare volume (m^3)	0.2115	0.0339

Even with the correct mass scaling, the two-dimensional model is not guaranteed to accurately reflect the behavior of the penetrator after impact. According to fluid dynamics, the drag coefficients of a cylinder and a flat plate bear no resemblance to each other because streamlines around the cylinder look completely different from the straight stagnation streamlines that have no way to bypass the flat plate. Similarly, the three-dimensional cylinder may offer less resistance than the two-dimensional plate passing through the snow. Additional analysis is required to determine whether or not the two-dimensional model reflects reality closely enough to give useful results.

The domain of the snow pack is relatively small since the number of elements grows as the cube of side length. Three elements span the surface layer vertically, while 22 elements span the underlying bulk snow. In order to control for all variables other than the dimensionality of the problem, the two-dimensional model uses a snow pack of the same size and mesh settings as the three-dimensional model. The materials of the surface layer and the bulk snow are both set to snow of density 440 kg/m^3. The three-dimensional and two-dimensional meshes are visible in Figure 4-37.

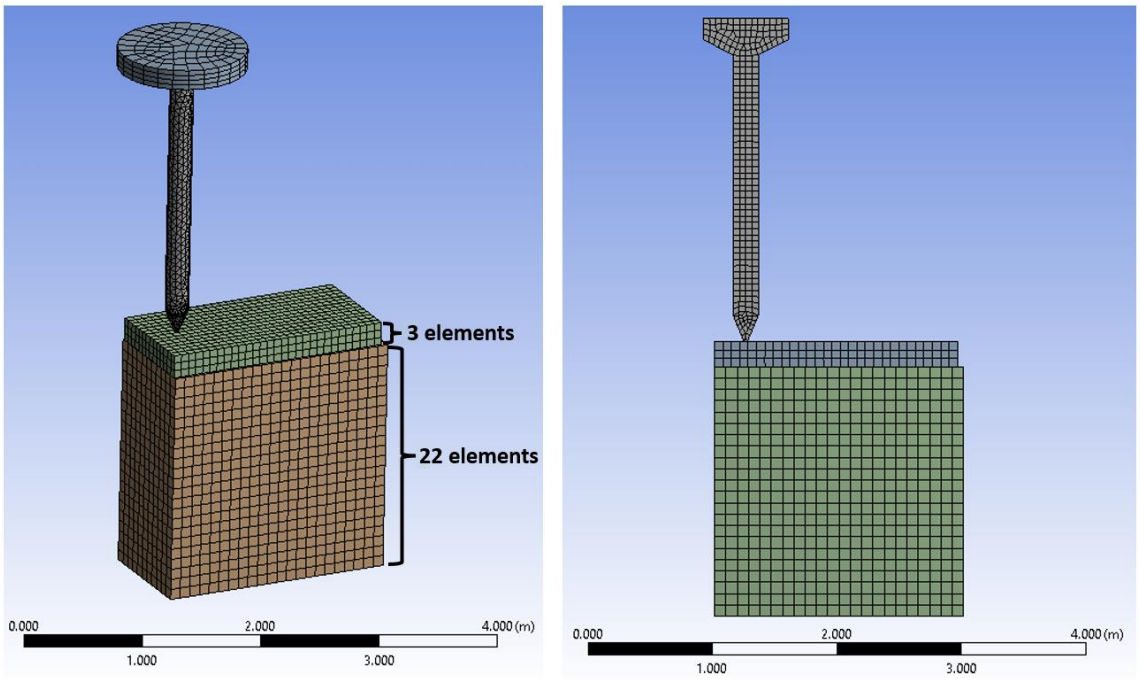


Figure 4-37. 3D and 2D meshes in ANSYS.

Figure 4-38 below shows the three-dimensional ANSYS result for a horizontal velocity of 2.5 m/s. The frames are separated by 20 ms and span the first 60 ms following initial contact of the penetrator and the snow pack. Figure 4-39 shows the same four frames for the two-dimensional result. The difference in solve time is rather dramatic – the author's machine with 32 GB of RAM running eight cores at 2.60 GHz solves the three-dimensional model in two hours, and the two-dimensional model in two minutes.

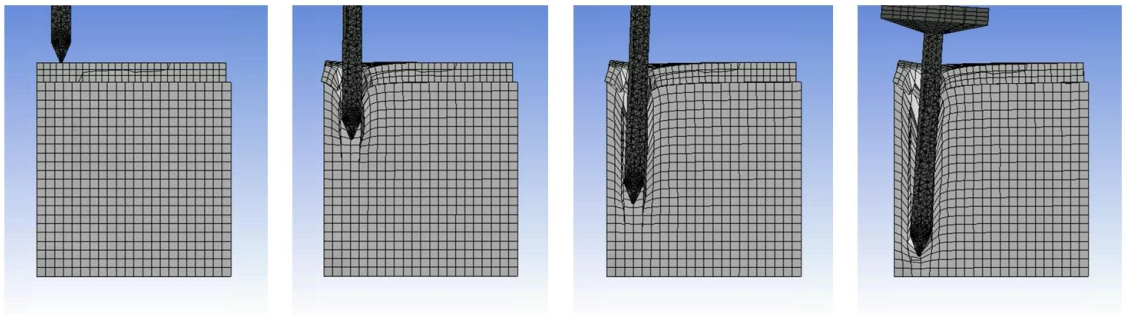


Figure 4-38. 3D ANSYS result, $V_Y = -42.5\frac{m}{s}, V_X = 2.5\frac{m}{s}$.

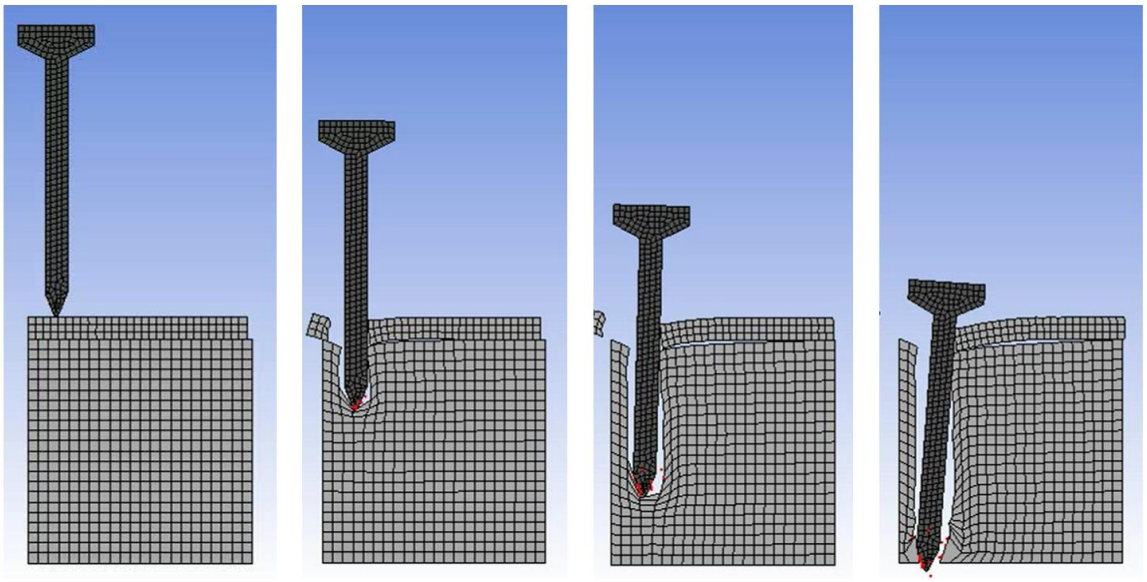


Figure 4-39. 2D ANSYS result, $V_Y = -42.5\frac{m}{s}, V_X = 2.5\frac{m}{s}$.

The two-dimensional and three-dimensional results outlined above appear almost indistinguishable, but visual inspection will yield only a qualitative answer. The angle of the penetrator as a function of time can be used to compare the two cases quantitatively.

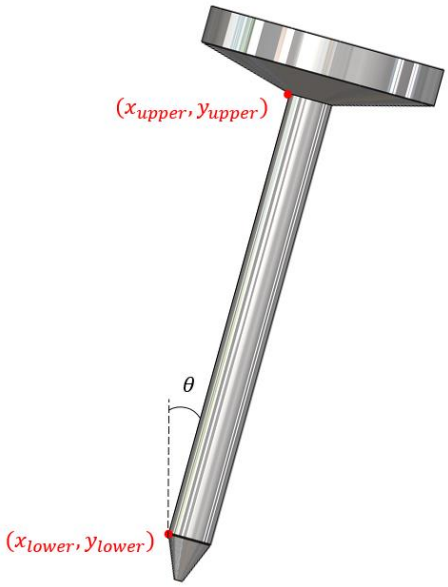


Figure 4-40. Angle off vertical during tipping.

ANSYS allows the user to track the locations of individual vertices. The lower and upper vertices shown in Figure 4-40 are perfectly aligned when the penetrator is

oriented vertically, so they can be used to define the penetrator's angle measured from the vertical axis. The angle is given by

$$\theta = \tan^{-1}\left(\frac{x_{upper} - x_{lower}}{y_{upper} - y_{lower}}\right) \qquad 4\text{-}12$$

and can be tracked throughout the impact event. Results for horizontal velocities ranging from 2.5 to 30 m/s are shown below in Figure 4-41 to Figure 4-47. Here, $\Delta\theta$ is given by $\theta_{3D} - \theta_{2D}$. Note from the last frame of Figure 4-39 that the value of θ will only be useful for times up to 60 ms, or 0.06 s. After 0.06 s, the penetrator reaches the fixed boundary at the bottom of the snow pack, and the position of the penetrator becomes influenced by unrealistic edge effects. The snow pack is kept small in this analysis, because as stated, any increase in the number of mesh elements causes a drastic increase in the computational time required for the three-dimensional model. However, future work would benefit from a larger model with a finer mesh.

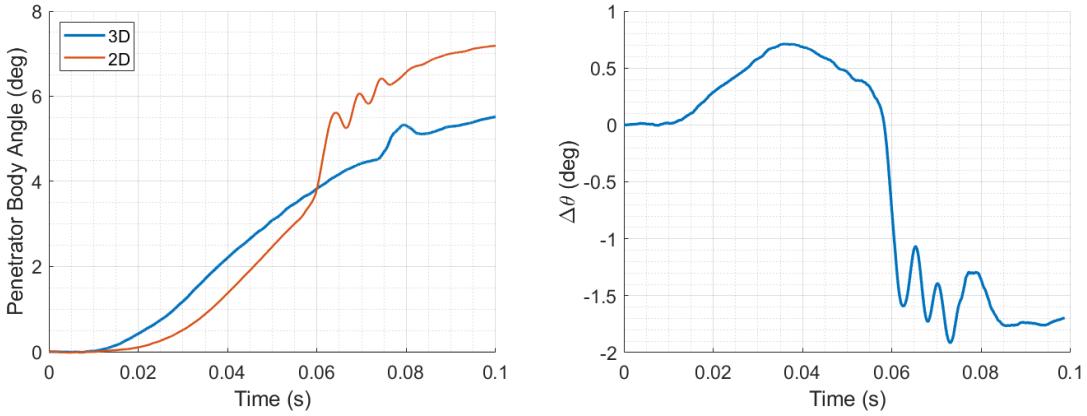


Figure 4-41. Penetrator angle for 3D and 2D cases, $V_X = 2.5\frac{m}{s}$.

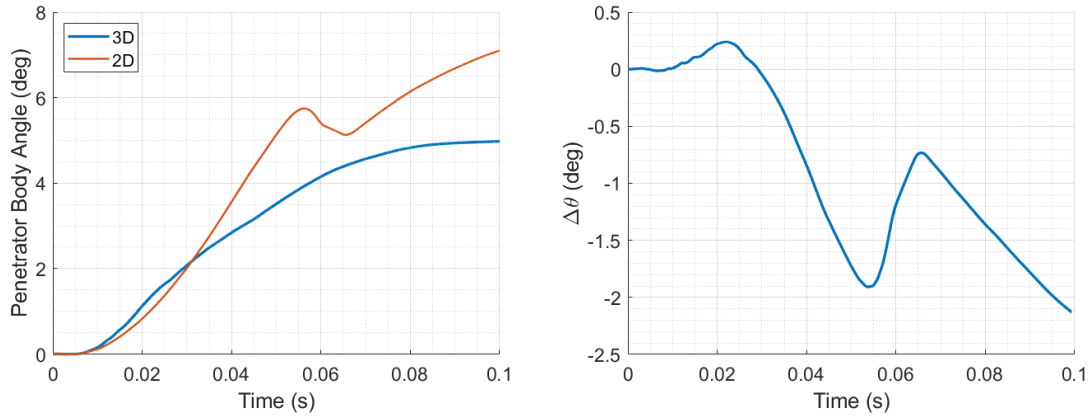


Figure 4-42. Penetrator angle for 3D and 2D cases, $V_X = 5\frac{m}{s}$.

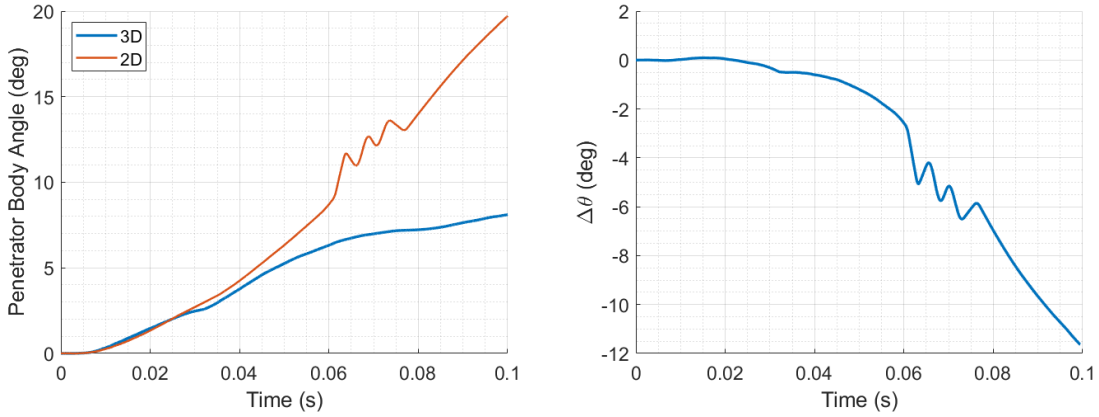


Figure 4-43. Penetrator angle for 3D and 2D cases, $V_X = 7.5\frac{m}{s}$.

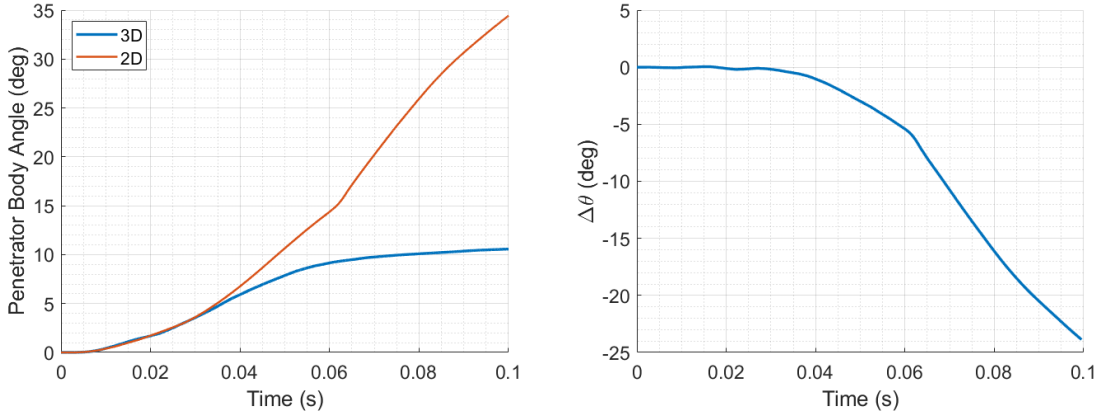


Figure 4-44. Penetrator angle for 3D and 2D cases, $V_X = 10\frac{m}{s}$.

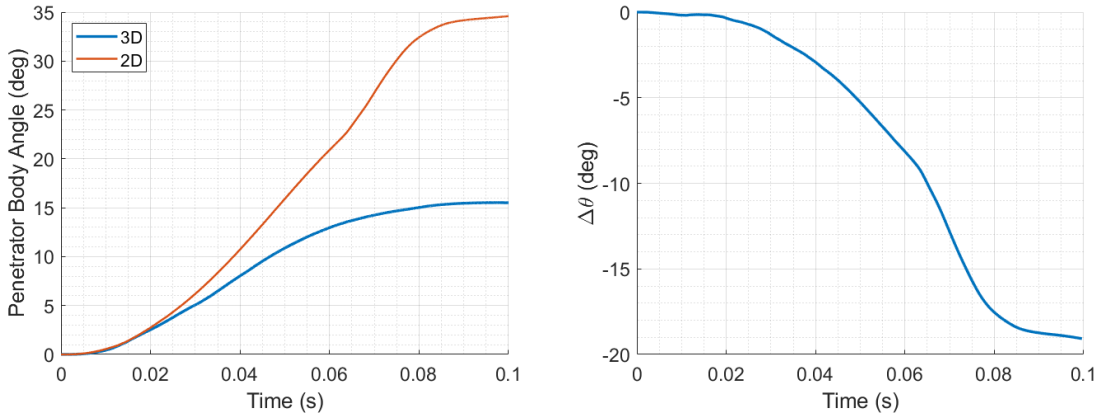


Figure 4-45. Penetrator angle for 3D and 2D cases, $V_X = 15\frac{m}{s}$.

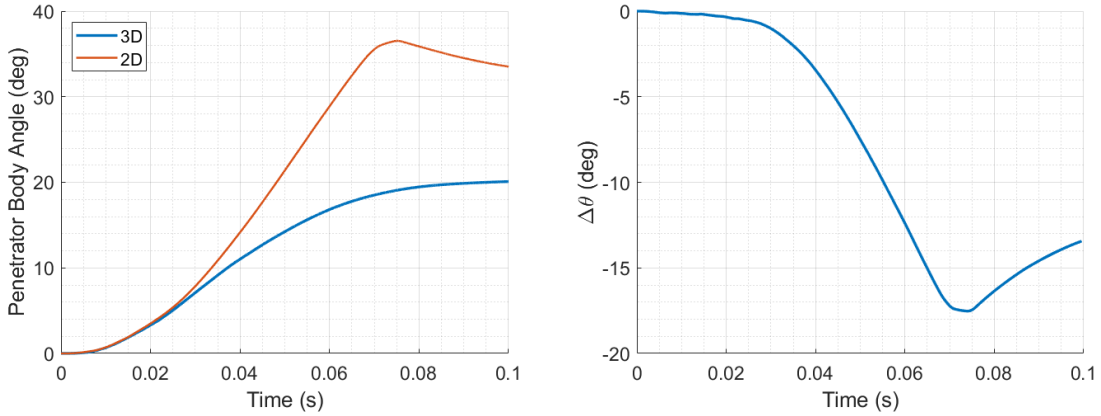


Figure 4-46. Penetrator angle for 3D and 2D cases, $V_X = 20\frac{m}{s}$.

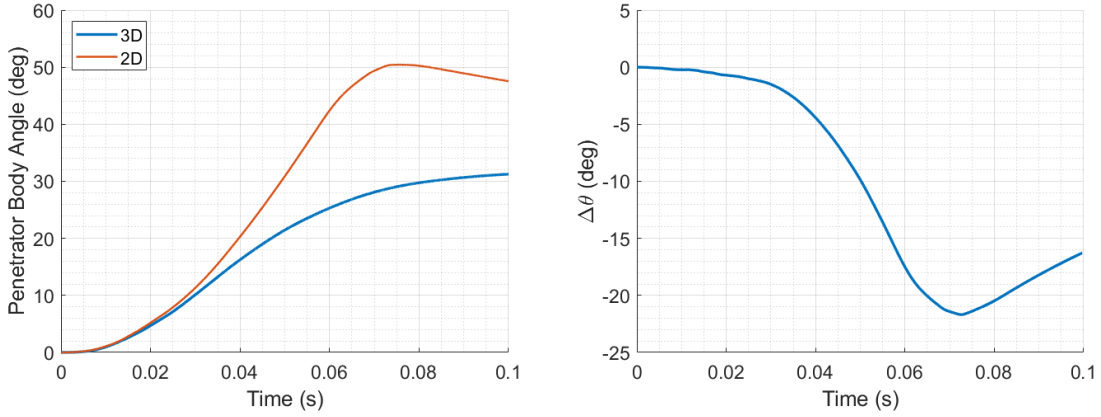


Figure 4-47. Penetrator angle for 3D and 2D cases, $V_X = 30\frac{m}{s}$.

Since the values of θ are realistic only up until $t = 0.06\,s$, the maximum realistic difference in angle can be considered to be that occurring before $t = 0.06\,s$ (see Figure 4-48).

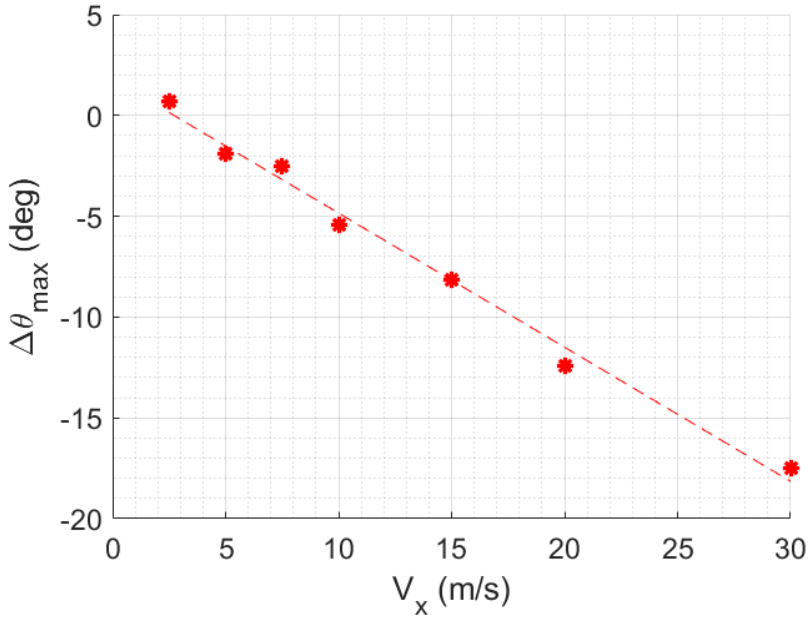


Figure 4-48. Max difference between θ_{3D} and θ_{2D} occurring before $t = 0.06\,s$.

The maximum difference in angle closely follows the linear relationship

$$\Delta\theta_{max} = -0.665V_x + 1.809 \qquad 4\text{-}13$$

Given the predictable differences between the two-dimensional and three-dimensional models, an argument may be made to use the faster two-dimensional model to produce useful results. However, caution must be undertaken. Before any decisions are based off of the two-dimensional model, the author recommends further work to compare larger models so that edge effects do not come into play.

In general, edge effects play a much larger role in the two-dimensional model. The three-dimensional penetrator barely reaches any edge for any horizontal velocity. As such, the three-dimensional analysis is expected to be more trustworthy. With a horizontal velocity of 10 m/s, the three-dimensional penetrator tips to a maximum angle of 10.6 degrees after 0.1 seconds. The maximum angle drops to 8.1 degrees if the horizontal velocity is instead 7.5 m/s. The simulations investigating the effects of horizontal velocity were run for 0.1 seconds, sufficient time to bring the three-dimensional penetrator to an almost complete, although not perfect, rest.

Extrapolating the three-dimensional data in Figure 4-42 to Figure 4-47 indicates less than one degree of additional tilt past 0.1 seconds. Given the seismometer-driven requirement to emplace the penetrator into the snow pack at an angle within 10 degrees off vertical [4], a maximum wind velocity of 7.5 m/s is recommended for drop operations.

The Trillium seismometer can be equipped with a self-righting gimbal that can level the instrument from all angles up to 105 degrees from vertical [32], but a hard impact has the potential to damage or disrupt the gimbal's ability to re-orient the seismometer. Additionally, the penetrator should be rigidly coupled to the snow pack after impact such that it will be able to detect any and all movement of the ice shelf. The higher the horizontal velocity at impact, the longer and shallower the horizontal swath plowed through the snow by the penetrator, and the less rigid the coupling of the penetrator body with the snow pack. Finally, regardless of the gimbal's ability to right the seismometer, the flare should be emplaced on the surface as close to vertical as possible. Thus, the requirement to keep the penetrator body within 10 degrees of vertical is kept, suggesting that drop operations should be undertaken only if wind speeds do not exceed 7.5 m/s.

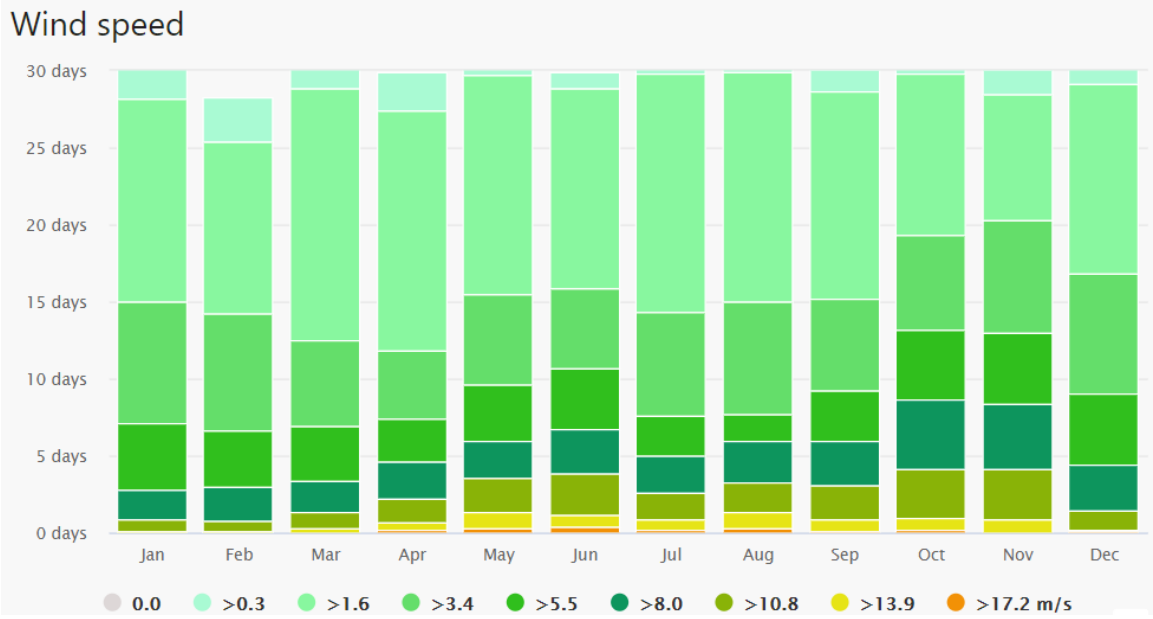


Figure 4-49. Meteoblue wind model for McMurdo Station [33].

A maximum wind speed requirement of 7.5 m/s means that high winds will cause a drop operation to stand down on the order of once every ten days. A Meteoblue weather model based off of 30 years of observation predicts that in winter (Antarctic summer) months on average, wind speeds at McMurdo Station will exceed 8 m/s on only three out of thirty days [33]. If the maximum wind speed is decreased further, the number of days available for launch will also start to decrease. Naturally, if the terminal velocity of the penetrator is decreased by using a larger flare, the wind speed causing the penetrator body to tip by an angle of 10 degrees or more will also decrease. Thus, a terminal velocity of 42.5 m/s is found to strike a reasonable balance between shock loading on impact, adequate penetration depth, and a resting orientation as close to vertical as possible.

5. Matsushima Penetrator Comparison

The Japanese Antarctic expedition as documented by Matsushima et al. generated useful data that can be used to ground the simulation results of this study. Details of the Matsushima penetrator geometry are provided in the paper, and are shown below. The penetrator mass is 14.5 kg.

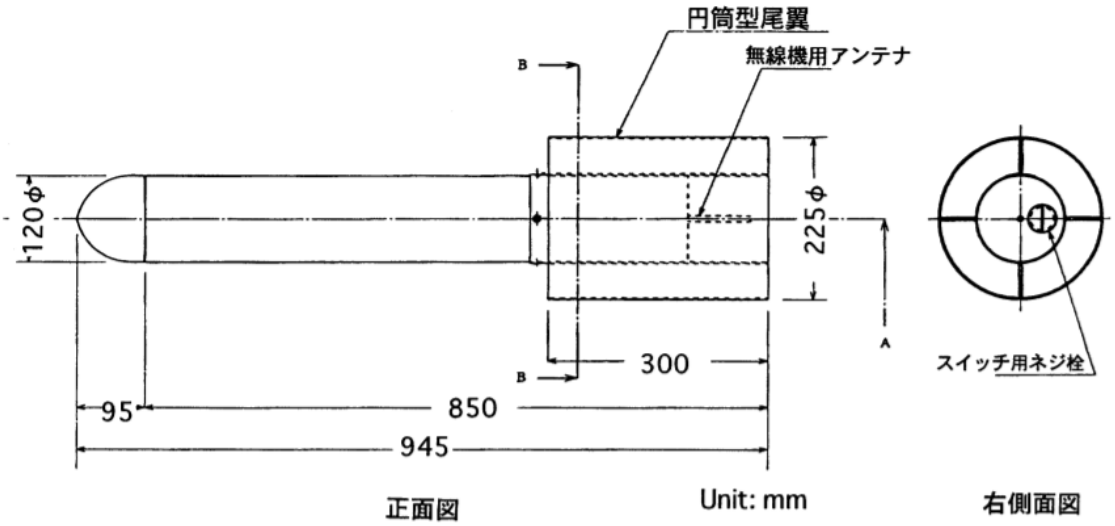


Figure 5-1. Details of Matsushima penetrator geometry [14].

The paper does not provide information on the penetrator's velocity at impact, but does give the drop altitudes. Two drops are of particular interest – those that impacted with zero angle of attack. These two drops are indicated with red arrows in Table 5-1, shown below with the titles of three columns of interest translated from Japanese. A drop from 149 m resulted in a penetration depth of 1.25 m, and a drop from 200 m resulted in a penetration depth of 1.45 m. Following the linear fit given in Figure 2-2, the 200 m drop is expected to experience an average shock load of 143 G, while the 149 m drop should experience an average of 122 G. Both impacts are simulated in ANSYS, but first, the velocity at impact must be calculated.

Table 5-1. Conditions of Matsushima penetrator drops [14].

Drop altitude Penetration depth Impact angle

実施日	投下時刻 (LT)	号機	衝撃センサ	投下地点	対地高度	対地速度	先端深度	着地傾度	地上風 気温
Dec 27 2001	1057:26 1101:51 1108:27	Dmy A Dmy B Dmy C	2 個 1 個 1 個	S16 S16 S16	100 m 74 m 138 m	W1 m/s E1 m/s E2 m/s	115 cm 75 cm 95 cm	14 度 45 度 7 度	NE8 m/s −4.5℃
Jan 03 2002	1452:53 1459:41 1505:25	Dmy A Dmy B 19		S30 S30 S30	104 m 105 m 101 m	W2 m/s W2 m/s SW1 m/s	115 cm 90 cm 140 cm	未測定 約 45 度 未測定	Calm
Jan 06	0954:45 1004:47 1013:58 1020:39 1028:56 1036:42	10 08 07 22 17 13	2 個	P01 P02 P03 P04 P05 P06	150 m 149 m 126 m 134 m 149 m 200 m	SE3 m/s W1 m/s SW2 m/s SE2 m/s W3 m/s SE1 m/s	115 cm 125 cm 120 cm 105 cm 135 cm 145 cm	30 度 0 度 20 度 20 度 15 度 0 度	E8 m/s −14℃
Jan 16	0924:02	21		SP4	268 m	W1 m/s	160 cm	14 度	E7 m/s
Jan 22	0959:17 1017:34 1035:51	Dmy 05 Dmy 03 Dmy C	2 個 2 個	S30 S30 S30	301 m 466 m 565 m	E6 m/s E6 m/s E1 m/s	145 cm 170 cm 180 cm	13 度 4 度 4 度	E8 m/s
Jan 23	1336:47 1348:24	18 Dmy 15		S30 S30	151 m 290 m	E2 m/s W5 m/s	135 cm 175 cm 以上	3 度 未測定	Calm

In order to calculate the resulting velocity at impact, the first step is to recreate a CAD model of the penetrator, shown below.

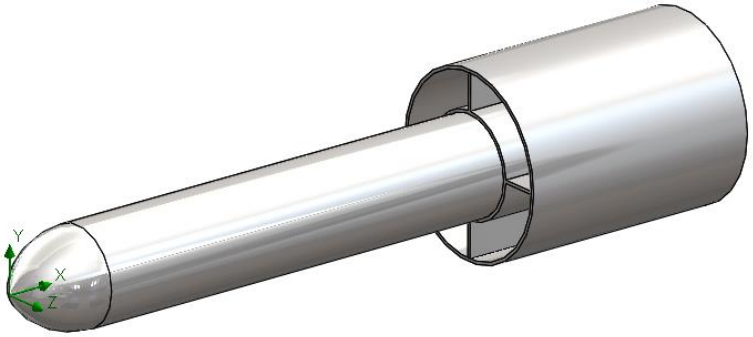


Figure 5-2. CAD recreation of Matsushima penetrator.

SolidWorks Flow Simulation is used to calculate the drag on the Matsushima penetrator at velocities ranging from zero to 70 m/s. The upper bound is chosen because in the absence of air drag, a pure ballistic trajectory from 200 m would result in a velocity of 62.6 m/s. Once again, the SolidWorks Flow Simulation mesh is adaptively refined, and has a maximum fluid cell count of 10^6.

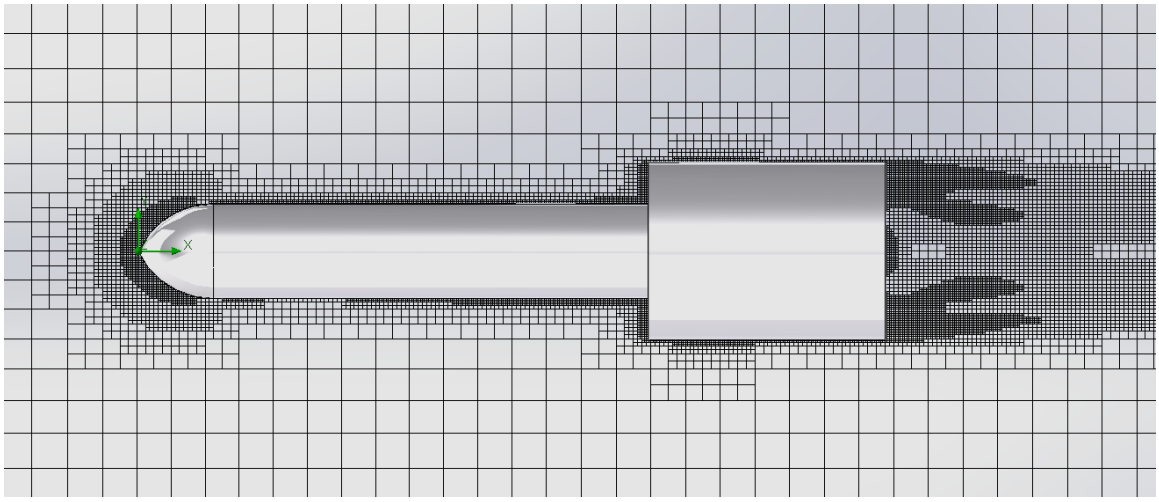


Figure 5-3. SolidWorks Flow Simulation mesh for Matsushima penetrator.

Figure 5-4 shows the pressure contours and streamlines resulting from 60 m/s airflow over the penetrator.

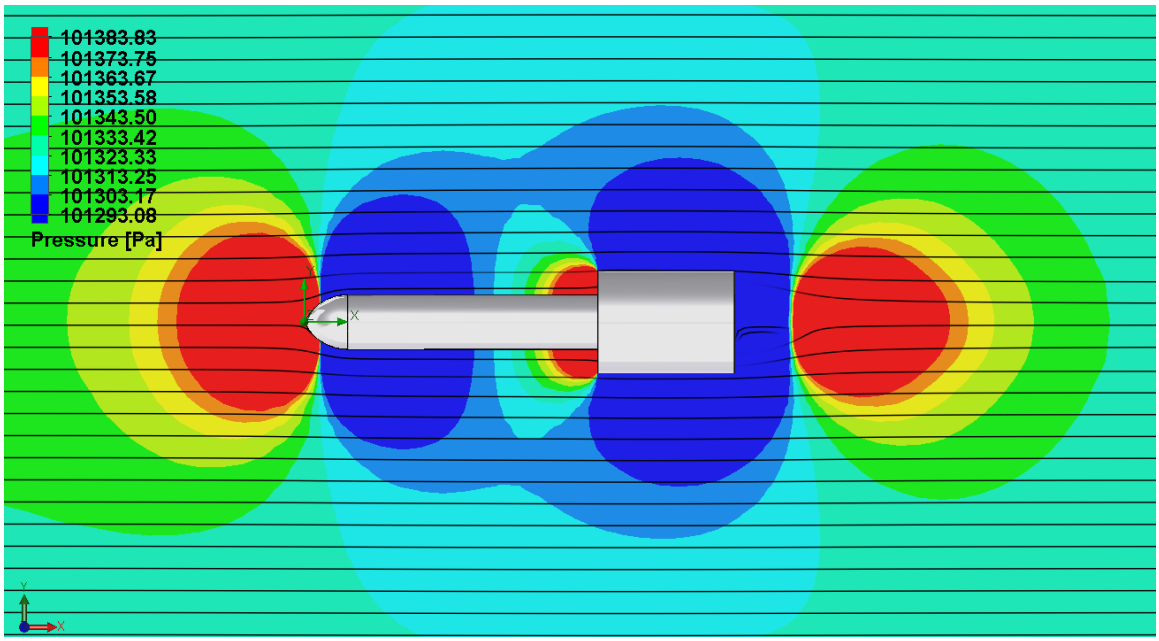


Figure 5-4. Pressure contours for Matsushima penetrator at 60 m/s.

Aerodynamic simulations are run at zero angle of attack in increments of 10 m/s up to 70 m/s. Then, drag values for all intermediate velocities are filled in via spline interpolation in MATLAB. The resulting relation between drag and velocity is shown in Figure 5-5. Even at 70 m/s, the drag is an order of magnitude lower than the penetrator's weight, suggesting that the terminal velocity of the Matsushima penetrator is far higher than that of the penetrator in this study.

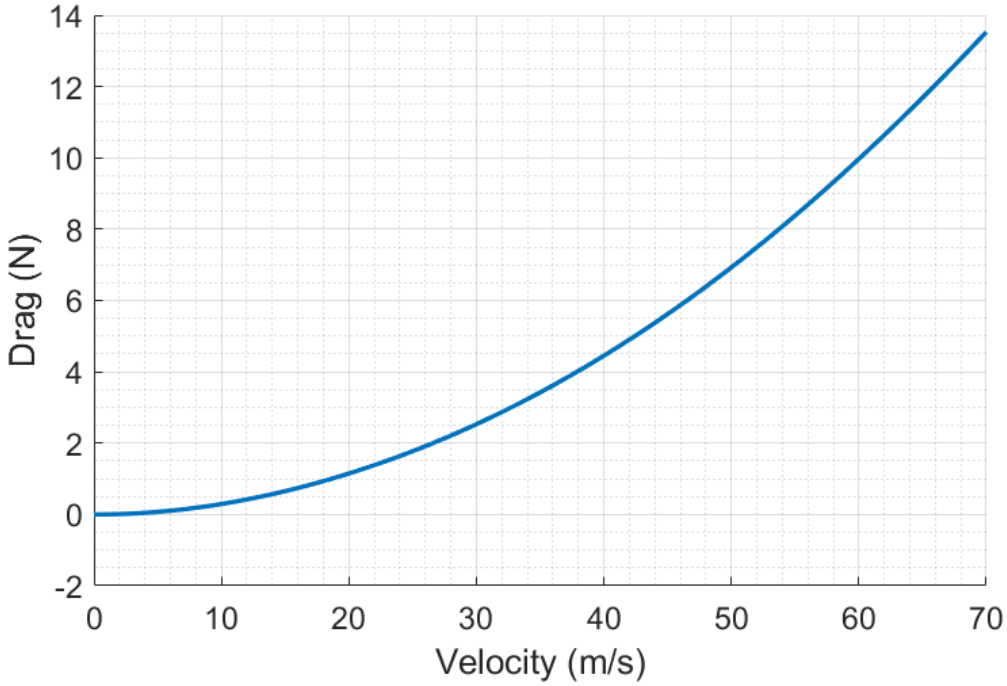


Figure 5-5. Drag vs. velocity for Matsushima penetrator.

With a lookup vector for drag established, the position and velocity of the penetrator can be numerically integrated over the duration of a drop. The impact velocities for drops from 200 and 149 m are tabulated in Table 5-2.

Table 5-2. Drop altitude and impact velocity of Matsushima penetrator.

Drop altitude (m)	Impact velocity (m/s)
200	61.56
149	53.40

Next, the impact velocity is input into an axisymmetric ANSYS simulation. The geometry and axisymmetric mesh used for the impact simulation are shown in Figure 5-6.

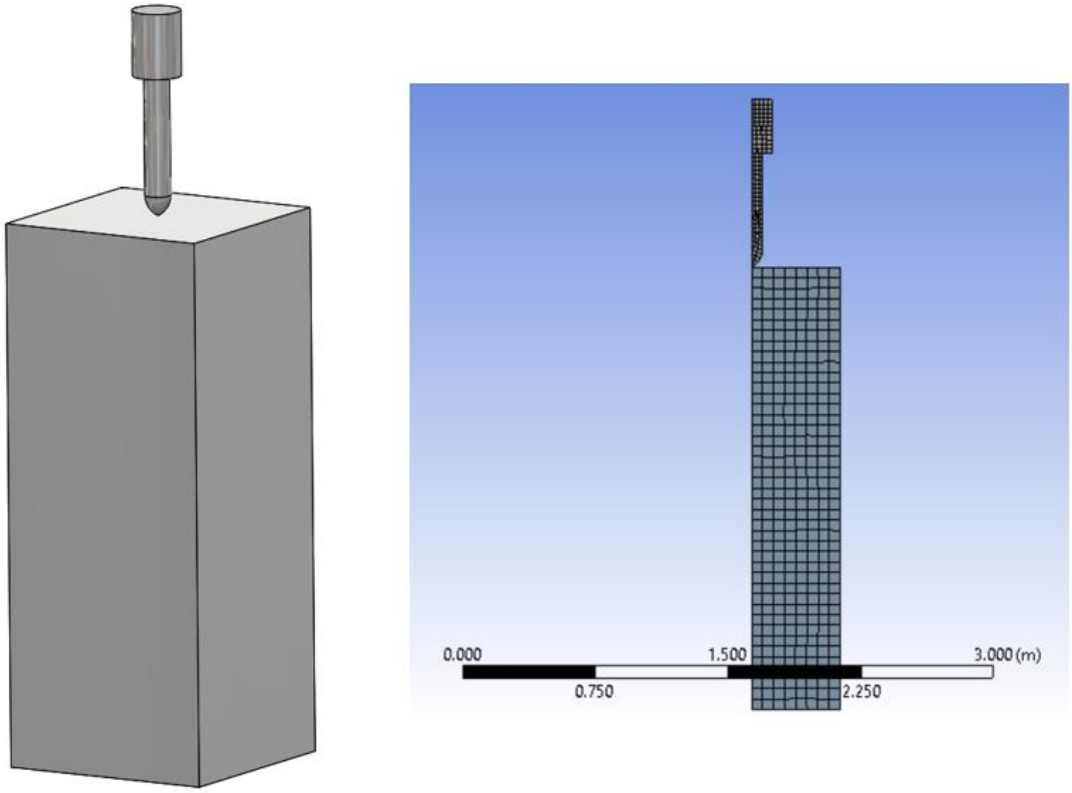


Figure 5-6. Matsushima impact geometry and axisymmetric mesh.

The position, velocity, and acceleration data of the penetrator as calculated by ANSYS are shown in Figure 5-7 and Figure 5-8 below. The penetration depth and shock load calculated by ANSYS are compared to the true values in Table 5-3.

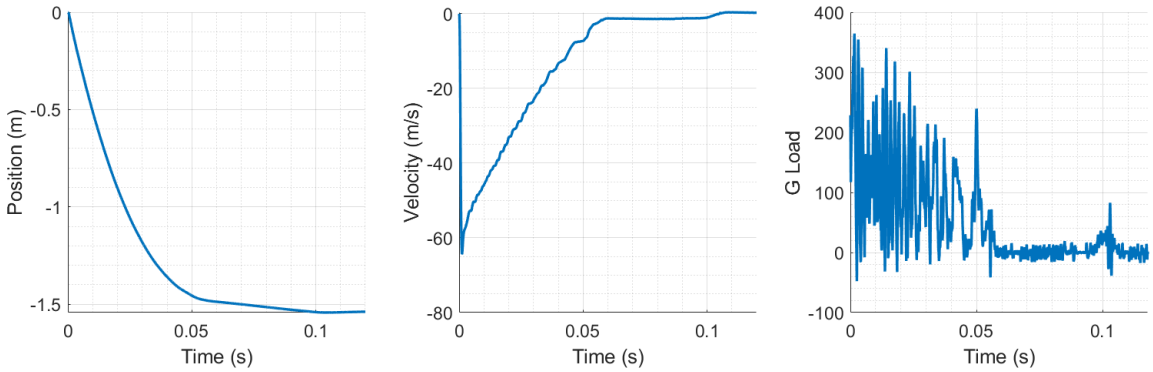


Figure 5-7. Position, velocity, and acceleration for 200 m drop altitude.

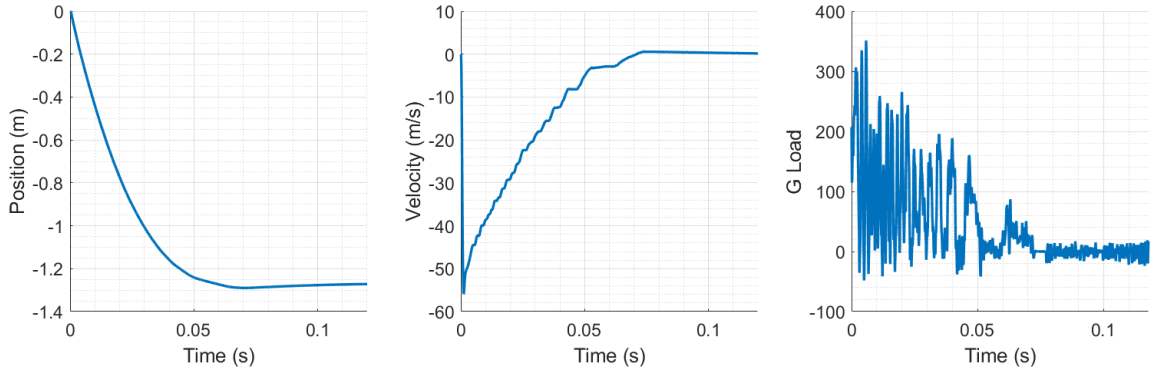


Figure 5-8. Position, velocity, and acceleration for 149 m drop altitude.

Table 5-3. Matsushima impact [14] and ANSYS comparison.

	Drop altitude (m)	Penetration depth (m)	Shock load (G)
True	200	1.45	143
ANSYS	200	1.54	365
True	149	1.25	122
ANSYS	149	1.27	351

The penetration depth calculated by ANSYS is remarkable close to the true value in both cases. For the drop from 200 m, ANSYS overpredicts the penetration depth by only 9 cm. Even more striking is the vanishingly small 2 cm overprediction for the 149 m drop case. The near-perfect match at the very least partially validates both the aerodynamic and impact-related computational models, increasing the confidence of accurately predicting the upcoming penetrator's performance in Antarctica.

At first glance, ANSYS seems to wildly overestimate the shock loading, but one must remember that the "true" shock loading values are averages calculated by the linear fit in Figure 2-2. The average values for deceleration over the entire impact duration, as calculated by ANSYS, are only 108 G and 96 G for the 200 m and 149 m drops, respectively.

6. Conclusion

6.1 Summary

A method for adjusting the penetrator flare geometry in order to converge to a desired terminal velocity is developed. Aerodynamic stability is analyzed for a velocity of 42.5 m/s, and is found to be relatively insensitive to the flare geometry. Therefore, a geometry may be chosen solely with respect to other factors, such as mechanical design considerations. The geometry considered for all analysis past section 3.5 is that with a flare cone angle of 75 ° and a cylinder depth 30% of the flare radius. This particular geometry results in a total penetrator mass of 92.2 kg.

Wind effects are considered, and reveal that the horizontal velocity of the penetrator is equal to the wind velocity at the moment of impact, as long as the drop altitude exceeds 2000-3000 ft (610-914 m). Other factors dictate that the drop altitude should be 4000 ft (1219 m) at the very minimum. The recommended drop altitude is at least 5000 ft (1524 m).

Impact simulations reveal that a terminal velocity of 42.5 m/s strikes a healthy balance between reasonable G loads (20 cm ice layer cases require special consideration), sufficient emplacement depth, and verticality of emplacement. At this velocity, a maximum wind speed of 7.5 m/s will keep the penetrator's emplacement angle into a pure snow pack below 10º. The maximum shock load on the flare is 566 G, and the maximum shock load on the body is 477 G. Thicker ice layers, if submerged, actually reduce the maximum G load on the flare since more of the penetrator's total kinetic energy is spent breaking through the ice before the flare impacts the surface. However, ice on the surface increases the maximum G loading felt by the flare.

Although they may decrease the shock loading on the flare, thicker ice layers definitely increase that experienced by the body. With a 20 cm ice layer, the body shock loading shoots well past 400 G, far in excess of what the seismometer can tolerate. However, the spikes are extremely fast, so they could feasibly be damped out by intelligently placed shock-absorbing materials in the penetrator body.

Finally, the computational methods used as part of this research are validated by comparing numerical results to field data collected during the JARE-43 summer operation [14].

6.2 Future Work

Much of the penetrator design process remains future work. Ongoing research is characterizing the thermal response of the power systems, penetrator structure, and interface between the snow pack and penetrator skin. Two undergraduates are working on selecting components for the avionics and data collection/telemetry subsystems, and two graduate students are set to start working on detailed penetrator design in the fall of 2021.

If the Iridium NEXT satellite network could be utilized in place of the traditional Iridium network, the power consumption of the penetrator could possibly be reduced. Any decrease in power consumption has the potential to dramatically reduce the penetrator mass, since lower power consumption translates to fewer batteries required to power all subsystems for one year. A significant mass reduction would result in a smaller flare required to produce the same terminal velocity, driving the mass down even further since the empty flares considered in section 3 alone weigh anywhere from 15 to 40 kg. However, if the penetrator mass is reduced by a large amount, the shock loading may increase. Thick ice layers may cause an excessively light penetrator to undergo intolerably high shock loading.

Reducing the penetrator length may help decrease the shock loading on the penetrator, since a lower terminal velocity could be used to emplace the shorter penetrator 1 to 1.5 body lengths into the snow pack. However, care must be taken. In the presence of a sufficiently thick (~20 cm) ice layer, reducing the drop velocity may not necessarily result in lower shock loading. Given the crack-softening failure model for ice, puncturing through an ice layer will spend a fixed amount of the penetrator's kinetic energy. Because of the V^2 dependence of kinetic energy on velocity, reducing the penetrator's kinetic energy by a fixed amount will correspond to a greater velocity change at lower velocities. For example, a 100 kg penetrator falling at 40 m/s has a kinetic energy of 80 kJ. Reducing the kinetic energy by 15 kJ brings the total down to 65 kJ, corresponding to a velocity of 36 m/s. However, if the penetrator instead falls at 20 m/s, its total kinetic energy is 20 kJ. The same 15 kJ decrease brings the velocity down to 10 m/s, causing a velocity change of 10 m/s as opposed to the previous 4 m/s.

Future work should thoroughly characterize the thicknesses and residing depths of any ice layers in the Ross Ice Shelf. Then, impact simulations using the true ice layer configuration of the Ross Ice Shelf should be run for various drop velocities

in order to understand the penetrator shock loading as a function of drop velocity. One complicating factor is the presence of ice lenses – localized ice layers only existing over small regions. If such lenses reside in the Ross Ice Shelf, the maximum ice thickness should be considered in the simulations. If sufficiently thick, work may have to be done to design effective shock absorbers to cushion the seismometer. Once the true ice layers are characterized, the tipping study should also be revisited since the ice layers may affect the penetrator's angle during impact.

References

[1] Delaney, A. J., Arcone, S. A., O'Bannon, A., and Wright, J. Crevasse Detection with GPR across the Ross Ice Shelf, Antarctica — IEEE Conference Publication — IEEE Xplore. https://ieeexplore.ieee.org/document/1343589. Accessed May 10, 2021.

[2] DeAgostini/Getty Images. Men Crossing Crevasses on Glacier Plateau. https://www.gettyimages.com/detail/news-photo/men-crossing-a-crevasses-on-the-glacier-plateau-overlooking-news-photo/630805251?adppopup=true&irgwc=1&esource=AFF˙GI˙IR˙Skimbit Ltd.˙10078&asid=Skimbit Ltd.&cid=GI&utm˙medium=affiliate&utm˙source=Skimbit Ltd.&utm˙content=10078. Accessed Apr. 26, 2021.

[3] Jauch Quartz GmbH. Lithium Thionyl Chloride Batteries from Jauch. https://www.jauch.com/en-INT/products/battery˙technology/getPrm/batteries/lithium thionyl chloride batteries/. Accessed May 13, 2021.

[4] Lowey, C. Design and Analysis of Penetrator Probes for Planetary Science Applications. https://dspace.mit.edu/handle/1721.1/113725. Accessed May 12, 2021.

[5] Nanometrics. Technical Specifications Trillium Compact. https://www.nanometrics.ca/sites/default/files/2020-11/trillium˙compact.pdf. Accessed May 14, 2021.

[6] Crary, A. P. *Glaciological Studies of the Ross Ice Shelf, Antarctica, 1957-1960*. World Data Center A: Glaciology, American Geographical Society, 1962.

[7] Lorenz, R. D. "Planetary Penetrators: Their Origins, History and Future." *Advances in Space Research*, Vol. 48, No. 3, 2011, pp. 403–431. https://doi.org/10.1016/j.asr.2011.03.033.

[8] Li, J. C., and Ma, G. W. An Analytical Study to Predict Underground Explosion-Induced Ground Motion. *EUROCK*. https://onepetro.org/ISRMEUROCK/proceedings-abstract/EUROCK10/All-EUROCK10/ISRM-EUROCK-2010-067/38577. Accessed May 17, 2021.

[9] Rosenau, W. Special Operations Forces and Elusive Enemy Ground Targets: Lessons from Vietnam and the Persian Gulf War. *MR-1408*. https://apps.dtic.mil/sti/pdfs/ADA400746.pdf. Accessed May 17, 2021.

[10] Correll, J. T. Igloo White. *Air Force Magazine*. https://www.airforcemag.com/PDF/MagazineArchive/Documents/2004/November 2004/1104igloo.pdf. Accessed May 17, 2021.

[11] Williams, D. R. Mars 96 Orbiter. *NASA Space Science Data Coordinated Archive*. https://nssdc.gsfc.nasa.gov/nmc/spacecraft/display.action?id=1996-064A.

[12] Williams, D. R. Deep Space 2. *NASA Space Science Data Coordinated Archive*. https://nssdc.gsfc.nasa.gov/nmc/spacecraft/display.action?id=DEEPSP2.

[13] Shibuya, K., Kaminuma, K., Ito, K., Yamada, I., Ikami, A., Hitoshi, M., Fujimura, A., Tsukamoto, S., and Kanazawa, T. Planned Explosion Seismic Experiments in East Queen Maud Land Using a Penetrator. *Proceedings of the NIPR Symposium on Antarctic Geosciences*. https://nipr.repo.nii.ac.jp/?action=pages˙view˙main&active˙action=repository˙view˙main˙item˙detail&item˙id=2684&item˙no=1&page˙id=13&block˙id=104. Accessed May 17, 2021.

[14] Matsushima, T., Yamashita, M., Yasuhara, T., Horiguchi, K., Hiroki, M., Toda, S., Takada, M., Watanabe, A., and Shibuya, K. Observation Tests of the Antarctic Penetrator on the Mizuho Plateau in JARE-43 Summer Operation. *Nankyoku Shiryō (Antarctic Record)*. 3. Volume 47, 395–408. https://core.ac.uk/download/pdf/51488723.pdf. Accessed May 17, 2021.

[15] Jones, D. H., and Gudmundsson, G. H. "Aircraft-Deployable Ice Observation System (ADIOS) for Instrumenting Inaccessible Glaciers." *Journal of Glaciology*, Vol. 59, No. 218, 2013, pp. 1129–1134. https://doi.org/10.3189/2013JoG13J112.

[16] Mandell, G. K., Caporaso, G. J., and Bengen, W. P. *Topics in Advanced Model Rocketry*. 1973.

[17] The Vertical Flight Society. Helicopter Speed Records. *Vertiflite Magazine*. https://vtol.org/publications/vertiflite-magazine/speed-records. Accessed May 16, 2021.

[18] ANSYS Inc. ANSYS Explicit Dynamics Brochure. *2021*. https://www.ansys.com/content/dam/product/structures/ansys-explicit-dynamics-brochure-140.pdf. Accessed May 1, 2021.

[19] Miljkovic, K., Jones, A. P., and Price, M. High Velocity Impact Modelling of Ice into Ice: Application to Outer Solar System Landers and Penetrators. *European Planetary Science Congress*. Volume 5. https://api.semanticscholar.org/CorpusID:55131413. Accessed Apr. 26, 2021.

[20] Mellor, M. "Engineering Properties of Snow." *Journal of Glaciology*, Vol. 19, No. 81, 1977, pp. 15–66. https://doi.org/10.3189/s002214300002921x.

[21] Van Herwijnen, A., Gaume, J., Bair, E. H., Reuter, B., Birkeland, K. W., and Schweizer, J. "Estimating the Effective Elastic Modulus and Specific Fracture Energy of Snowpack Layers from Field Experiments." *Journal of Glaciology*, Vol. 62, No. 236, 2016, pp. 997–1007. https://doi.org/10.1017/jog.2016.90.

[22] Shapiro, L., Johnson, J., Sturm, M., and Blaisdell, G. Snow Mechanics: Review of the State of Knowledge and Applications. *CRREL Report*. https://www.researchgate.net/publication/235068191˙Snow˙Mechanics˙Review˙of˙the˙State˙of˙Knowledge˙and˙Applications. Accessed May 14, 2021.

[23] Sommerfeld, R. A. "The Relationship between Density and Tensile Strength in Snow." *Journal of Glaciology*, Vol. 10, No. 60, 1971, pp. 357–362. https://doi.org/10.3189/s002214300002205x.

[24] Capelli, A., Kapil, J. C., Reiweger, I., Or, D., and Schweizer, J. "Speed and Attenuation of Acoustic Waves in Snow: Laboratory Experiments and Modeling with Biot's Theory." *Cold Regions Science and Technology*, Vol.

125, 2016, pp. 1–11. https://doi.org/10.1016/j.coldregions.2016.01.004.

[25] Zhang, X., Huang, Y., Sun, P., Liu, X., Ma, Z., Zhou, Y., Zhou, J., Zheng, W., and Sun, C. Q. "Ice Regelation: Hydrogen-Bond Extraordinary Recoverability and Water Quasisolid-Phase-Boundary Dispersivity." *Scientific Reports*, Vol. 5, No. 1, 2015, pp. 1–8. https://doi.org/10.1038/srep13655.

[26] Camponovo, C., and Schweizer, J. "Rheological Measurements of the Viscoelastic Properties of Snow." *Annals of Glaciology*, Vol. 32, 2001, pp. 44–50. https://doi.org/10.3189/172756401781819148.

[27] Ligtenberg, S. R. M., Helsen, M. M., and Van Den Broeke, M. R. "An Improved Semi-Empirical Model for the Densification of Antarctic Firn." *The Cryosphere*, Vol. 5, 2011, pp. 809–819. https://doi.org/10.5194/tc-5-809-2011.

[28] National Science Foundation. 2019-2020 USAP Field Season Air Operations. https://www.usap.gov/sciencesupport/scienceplanningsummaries/2019˙2020/airoperations.cfm. Accessed May 1, 2021.

[29] Air Center Helicopters. Air Center Helicopters Capabilities Briefing. https://static1.squarespace.com/static/5913890e03596e07853b104e/t/60624cb59a80f316d9c1a979/1617054904030/DoD˙FactSheet˙final.pdf. Accessed May 1, 2021.

[30] Eurocopter. AS350-B3 Flight Manual. https://www.maunaloahelicopters.edu/library/Rotorcraft˙Flight˙Manuals/Airbus˙Eurocopter˙Helicopter/AS˙350˙B3.pdf. Accessed May 1, 2021.

[31] Bell Helicopter Textron. Bell 412 Rotorcraft Flight Manual. https://www.maunaloahelicopters.edu/library/Rotorcraft˙Flight˙Manuals/Bell˙Helicopter/412.pdf. Accessed May 1, 2021.

[32] Nanometrics. *Trillium Compact OBS User Guide*.

[33] Meteoblue. Climate McMurdo Station. https://www.meteoblue.com/en/weather/historyclimate/climatemodelled/mcmurdo-station˙antarctica˙6696480. Accessed May 12, 2021.